Three-Dimensional Finite Element Analyses of Tire Derived Aggregates in Ballasted and Ballastless Tracks

Mohammad Adnan Farooq[a], Sanjay Nimbalkar[b*], Behzad Fatahi[c]

[a]PhD Candidate, School of Civil and Environmental Engineering, University of Technology Sydney, Ultimo NSW 2007, Australia.

Email: MohammadAdnanFarooq@student.uts.edu.au

ORCID iD: 0000-0001-6211-7392

[b]*Corresponding author, Senior Lecturer, School of Civil and Environmental Engineering, University of Technology Sydney, Ultimo NSW 2007, Australia.

Email: Sanjay.Nimbalkar@uts.edu.au

ORCID iD: 0000-0002-1538-3396

[c]Associate Professor, School of Civil and Environmental Engineering, University of Technology Sydney, Ultimo NSW 2007, Australia.

Email: Behzad.Fatahi@uts.edu.au

ORCID iD: 0000-0002-7920-6946

Abstract

Scrap tyres are a significant source of pollution and pose a grave threat to the environment and human health. The present study aims to examine the application of Tyre Derived Aggregate (TDA) in a concrete slab track and ballasted track and compare its performance in both track forms. In this study, long-term performance of slab track and ballasted track subjected to train induced loading is demonstrated based on the three-dimensional finite element modelling. The most suitable constitutive hyperelastic model for TDA has been identified. Subsequently, the most suitable position for the location of TDA is determined for both track types. A comparative analysis between slab track and ballasted track, with and without TDA, is presented in terms of stress transfer, vibration reduction and displacement (elastic and plastic). It is shown that TDA helps in reducing up to 50% vibration levels of both track types. The influence of train speed and axle load on the vertical and horizontal displacement and stress response of both track forms is shown for a large number of load cycles. Overall, it is observed that the long-term performance of TDA is better in slab track compared to ballasted track.

Keywords: Tyre derived aggregates, finite elements, slab track, ballasted track, scrap rubber

1. Introduction

The railway tracks have been under development since their inception, and their components are modified to satisfy various design requirements. There are two types of railway tracks: ballasted and ballastless (also known as slab track). In traditional ballasted track, the rails are attached to sleepers, which are cushioned by crushed rocks called ballast. However, in a slab track, the rails are fixed to the concrete slab. The ballasted railway track has been the most preferred railway track owing to its low initial construction cost and ease in maintenance (Kaewunruen and Remennikov, 2008). However, they incur high maintenance cost as compared to the slab tracks (Bian et al., 2014; Woodward et al., 2014) and generally, show poor performance with increasing train speeds (Cebasek et al., 2018). This poor performance of ballasted track is due to reduction in resilient modulus of ballast with an increase in train speed (or loading frequency) (Sun et al., 2018). Besides, research has shown that the slab track proves to be more economical over a long period as compared to ballasted track (Schilder and Diederich, 2007). These factors have led to increased usage of slab tracks for high-speed railways across the globe. The low maintenance cost associated with a slab track is due to the absence of ballast, which has a major contribution towards settlement in a ballasted track (Li et al., 2016). Although maintenance requirement is significantly reduced in a slab track, it should be ensured that differential settlement does not occur; otherwise, significant damage can occur to the concrete slab (Cebasek et al., 2018).

The noise and vibration problem are among the significant drawbacks associated with a High-Speed Rail (HSR). The stiffness of the substructure of a HSR can impact the inception of vibration and its transmission to the subgrade (Ho et al., 2013). During the past few years, resilient materials, such under-sleeper pads and ballast mats are being used in railway tracks (Alves Costa et al., 2012; Navaratnarajah and Indraratna, 2017; Nimbalkar et al., 2012; Sol-Sánchez et al., 2015a). These resilient materials with higher damping characteristics aid in

better energy dissipation, increased contact area, and reduced stresses, which minimise the track damage (Abadi et al., 2015; Indraratna et al., 2014; Sol-Sánchez et al., 2015a).

Presently, various elastic elements, such as under-sleeper pads, Under-Ballast Mats (UBMs) and other new materials are being used as an isolation layer in the railway track. Waste tyres represent one of the most eminent elastic wastes used to manufacture railway pads (Sol-Sánchez et al., 2014). Different materials are used as an isolation layer, for example China railway track system III uses Ethylene Propylene Diene Monomer (EPDM), geotextile, and polyethylene film as an isolation layer. The main functions of the isolation layer include limiting the deformation between the concrete slab and underlying components, providing easy maintenance options, and reducing the vibration and noise (Sheng et al., 2020). Recently, a study investigated the use of UBM rubber as an isolation layer in a slab track and concluded that proper selection of UBM is required to achieve the desired performance (Sheng et al., 2020).

Globally, around 1.5 million tyres are manufactured each year (Pelisser et al., 2011; Song et al., 2019). It is estimated that in some cities of the United States, such as California 40 million tyres (Ghaaowd et al., 2017), and in Australia approximately 50 million tyre equivalent passenger units are discharged each year (Indraratna et al., 2017). The annual production of tyre-derived material in Europe and USA is 6.4 and 12.6 kg/resident/year, respectively (Rodríguez et al., 2018). Lately, the accumulation of waste tyres across the globe has necessitated the reuse of scrap tyres in the construction industry. It is known that construction of embankment over soft soil is problematic due to low bearing capacity (Meena et al., 2020). Consequently, the recycled tyres have been used in the construction of embankments over soft soils. Recycled tyres have performed similar or better than the conventional fill (Meles et al., 2013; Mills and McGinn, 2010). Besides, studies have been carried out on the application of recycled tyres or Tyre-Derived Aggregates (TDA) in ballast and sand (Asadi et al., 2018; Fathali et al., 2017; Ghazavi, 2004; Jamshidi Chenari et al., 2019, 2017; Sol-Sánchez et al.,

2015a). Some studies suggest that the addition of 10% TDA by weight reduced the ballast particle breakage and settlement by 47% and 6%, respectively (Fathali et al., 2017). Moreover, the track settlement reduced on the addition of 10% crumb rubber by volume in ballast (Sol-Sánchez et al., 2015b). However, other studies report enhancement in settlement of sand fouled ballast by 142%, 280%, and 633% on addition of TDA in 5%, 10%, and 15% (by weight), respectively (Esmaeili et al., 2017), which suggests a discrepancy in the results of available literature on the use of TDA in ballast, demanding further and more in-depth research in this area.

Numerical modelling has proved to be very useful in evaluating the performance of railway tracks. Numerical modelling has been used to study the behaviour of ballasted track embedded with geocell at the interface of ballast-subballast layer, and it has shown promising results in reducing vertical deformations (Leshchinsky and Ling, 2013). A multi-model framework consisting of analytical, hybrid analytical-numerical, 2.5D numerical and 3D numerical approach has been used to develop further understanding of railway ground dynamics (Connolly et al., 2020). Recently, numerical modelling has been used to capture the behaviour of full-scale structures under cyclic loading. The short-term behaviour of the railway track was assessed by calibrating the Young modulus and Poisson's ratio of various track layers till the displacement output of the numerical model matched with the experimental results. The long-term behaviour of the railway tracks was simulated by calibrating the empirical permanent deformation model (Ramos et al., 2021). Finite Element (FE) analysis has been employed to evaluate the impact of varying TDA proportion, TDA aspect ratio, and relative density on the settlement of TDA-sand mixture (Jamshidi Chenari et al., 2017). FE analysis has also been used to develop design charts for the use of TDA in highway embankments (Meles et al., 2016). Studies using the technique of numerical modelling have been performed to investigate the dynamic response of a TDA-ballasted track. The ability of TDA in reducing vibrations has been demonstrated by some studies (e.g., Wolfe and Humphrey, 2000). While some FE studies

consider TDA mixed with ballast in varying proportions (Esmaeili et al., 2017), others use TDA as a layer below the ballast layer (Humphrey and Blumenthal, 2010). Esmaeili et al. (2020) used TDA as subballast over a bridge structure and observed up to 63% reduction in peak acceleration of the sleeper, depicting the excellent performance of TDA in vibration reduction. However, as per the authors' knowledge, there is no previous FE study on the use of TDA in a slab track.

Most of the previous studies model TDA as an elastic material (Gong et al., 2019; Jamshidi Chenari et al., 2017) and few studies (Ni et al., 2018) consider TDA as a hyperelastic material. However, as per the authors' knowledge, previous studies do not specify the most suitable hyperelastic constitutive model (strain energy potential) for TDA. The present study attempts to determine the most suitable hyperelastic model for TDA in ABAQUS.

From the preceding paragraphs, it is evident that while a lot of studies have explored the use of various elastic elements such as under-sleeper pads, UBMs, geotextile, EPDM, and polyethylene in ballasted and slab tracks, few studies have investigated the use of TDA in a ballasted track and as per authors' knowledge no investigation has been performed on the use of TDA in a slab track.

The three-dimensional (3-D) finite element models of the ballasted and slab tracks have been developed using the finite element software, ABAQUS (Dassault Systems, 2018). The distribution of stress and displacement has been shown for both track types. Hyperelastic model has been used for TDA and validated against a one-dimensional study on the compression behaviour of TDA (Meles et al., 2013). The influence of TDA on the track response is investigated by introducing it at different positions in the ballasted and slab tracks. The most suitable location for the placement of TDA is then determined for ballasted and slab track based on maximum allowable displacement. A parametric study has been conducted to evaluate the influence of train speed and axle load on the performance of slab track and ballasted track, with

and without TDA. The developed models have been validated against previous experimental work of Cebasek et al. (2018).

2. Finite element (FE) analyses

2.1. Slab track and ballasted track geometry

The 3D models of a section of concrete slab track and the ballasted track were developed in ABAQUS software (Dassault Systems, 2018). The dimensions of various layers of a slab track, that is concrete slab, grout mass, base layer, subbase layer, and subgrade, are shown in Figure 1 (a). The dimensions of different layers of a ballasted track; viz. sleeper, ballast, subballast, and subgrade, are shown in Figure 1 (b). The length, width, and depth of the concrete slab is 2.8 m, 2 m, and 0.2 m, respectively. The distance between the rails is 1.435 m in both tracks. The sleepers are assumed to be embedded in the concrete slab of the slab track and are spaced 0.65 m centre to centre in both tracks. The cut rail parts used in both the tracks is 60E1 (UIC 60) confirming with British standard BS EN 13674-1 (2011).

2.2. Material models and properties

A majority of the material properties of various components of the slab track and ballasted track used in the FE analysis have been taken from the work of Cebasek et al. (2018), as shown in Table 1 and Table 2. The steel and concrete are modelled as elastic material as non-yielding behaviour is anticipated for rail, concrete slab, grout mass, and base layer. The subbase layer is modelled as non-associative elastic-plastic material, adhering to 3D Drucker-Prager (D-P) yield criterion. The subgrade layer is modelled as a linear elastic-perfectly plastic material with a Mohr-Coulomb failure criterion. The substructure in this study consists of limestone, which is a granular material, and it is known that the strength and yield of granular material depend on the volumetric strain and stress level. Previous studies report the use of D-P yield criterion to model granular materials; viz. ballast and subballast (Leshchinsky and Ling, 2013). The basic equations (equations A-1 to A-7) for the D-P model are given in Appendix. The friction

and dilation angle for the subbase, subballast, and subgrade are based on typical values for a hard limestone. The damping ratio for TDA has been adopted as 0.2 (Fox et al., 2018).

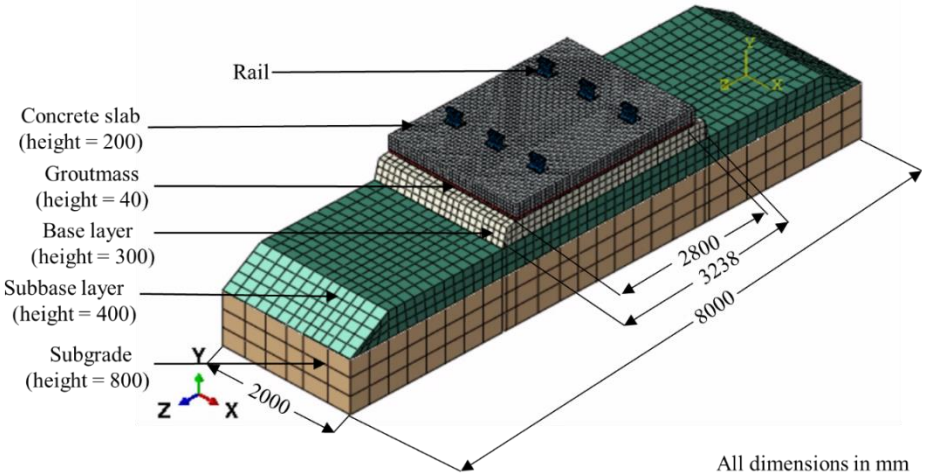

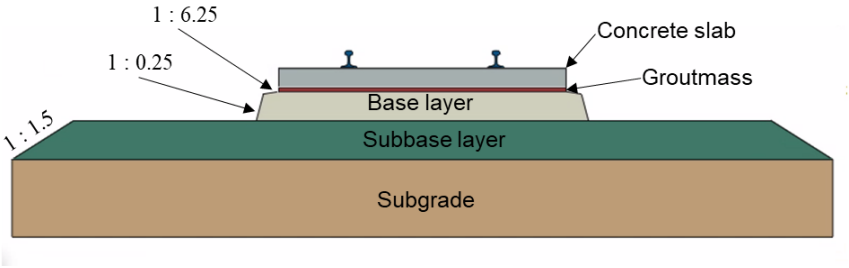

(a)

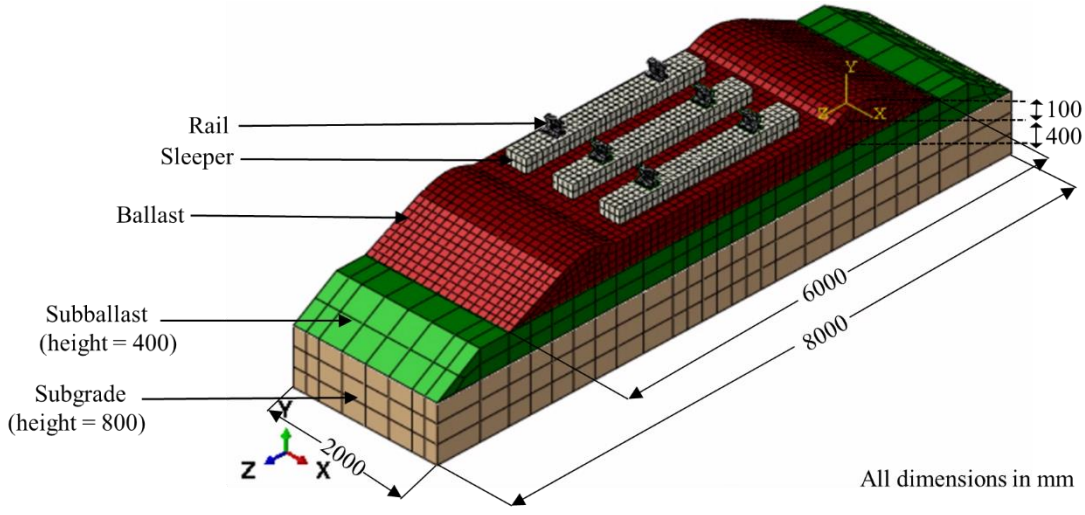

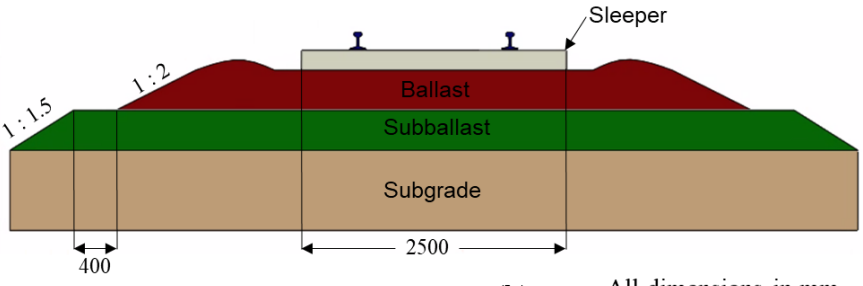

Figure 1. Isometric and the cross-sectional view of the superstructure and substructure modelled in ABAQUS (a) slab track (b) ballasted track

Table 1. Material parameters for a slab track (Cebasek et al., 2018; Hall, 2003)

Properties	Rail[1]	Concrete slab[1]	Groutmass[1]	Base layer[1]	Subbase layer[1]	Subgrade[1]
Constitutive model	Linear Elastic	Linear Elastic	Linear Elastic	Linear Elastic	Drucker-Prager	Mohr-Coulomb
Mass Density, ρ (kg/m^3)	7830	2700	2250	2700	2220	2220
Elastic Modulus, E (MPa)	210,000	20,000	27,000	7500	400	400
Poisson's Ratio, ν	0.3	0.167	0.167	0.167	0.25	0.25
Friction Angle, $\emptyset$	-	-	-	-	35	35
Dilation Angle, ψ	-	-	-	-	2	2
Damping Ratio, ζ	-	-	-	-	0.04[2]	0.04[2]

[1](Cebasek et al., 2018), [2](Hall, 2003)

Table 2. Material parameters for a ballasted track (Cebasek et al., 2018; Hall, 2003; Nimbalkar and Indraratna, 2016)

Properties	Rail[1]	Sleeper[1]	Ballast[1]	Geogrid[3*]	Subballast[1]	Subgrade[1]
Constitutive model	Linear Elastic	Linear Elastic	Drucker-Prager	Linear Elastic	Drucker-Prager	Mohr-Coulomb
Mass Density, ρ (kg/m^3)	7830	2400	1600	200**	2220	2220
Elastic Modulus, E (MPa)	210,000	30,000	110	210	400	400
Poisson's Ratio, v	0.3	0.15	0.3	0.33	0.25	0.25
Friction Angle, $\emptyset$	-	-	40	-	35	35
Dilation Angle, ψ	-	-	5	-	2	2
Damping Ratio, ζ	-	-	0.04[2]	-	0.04[2]	0.04[2]

*used for validation purpose,** based on the mass per unit area of 300 g/m^2 and thickness of 1.5 mm, [1](Cebasek et al., 2018), [2](Hall, 2003), [3](Nimbalkar and Indraratna, 2016)

2.3. FE mesh and boundary conditions

The slab track model consists of 15,116 elements and 26,972 nodes, while the ballasted track comprises 15,262 elements and 24,249 nodes. The 8–noded hexahedral linear brick elements (first-order) with reduced integration and hourglass control (C3D8R) elements are used in the analysis for both slab track and ballasted track. The reduced integration decreases the analysis time when solving the integral as it involves a reduced number of Gaussian co-ordinates. The pinned support boundary condition is used for the base of the slab track and ballasted track, and restricted from displacements in x, y, and z directions. The x-y and y-z planes of the slab track are restricted from displacement in z and x directions, respectively. The rail, concrete

slab, groutmass, base layer, subbase layer, and subgrade are assigned global element sizes of 0.05, 0.1, 0.1, 0.15, 0.15, and 0.3, respectively in a slab track. Similarly, the rail, sleeper, ballast, subballast, and subgrade are given global element sizes of 0.025, 0.075, 0.1, 0.3, and 0.6, respectively in a ballasted track. The mesh coarseness of various parts of the slab track increased from top to bottom layers to focus on more rigorous computational analysis of the top layers. Interaction between the various layers is modelled as surface-to-surface contact with "hard" normal contact and tangential behaviour as penalty with a coefficient of friction of 0.5. The rail pad was modelled as a spring with a stiffness of 22.5 kN/mm (Cebasek et al., 2018).

3. Stress transfer and displacement of ballasted and slab track

Figure 2 shows the comparison of stress transfer and vertical elastic displacement of various components of a ballasted and slab track. The maximum stress due to train load (wheel load = 58.86 kN) at the top of ballasted and slab track is approximately 5,400 kPa. It is evident that in a slab track, most of the stress is dissipated at 0.2 m depth from slab top whereas the same stress exists at 0.6 m from sleeper top in a ballasted track. This can be attributed to the higher toughness of reinforced concrete slab, which enhances its stress spreading ability and energy absorbing capacity. The stress level at the subgrade bottom is half in case of slab track (approximately 50 kPa) compared to ballasted track (approximately 100 kPa).

The vertical elastic displacement at the top of the slab track decreases by approximately 95% compared to ballasted track. The settlement in the ballasted track (7.86 mm) is around 26 times higher compared to slab track (0.3 mm) after the application of 1.2 million cycles, as shown in Figure 15. The strain level at the bottom of subgrade in both slab track and the ballasted track is negligible.

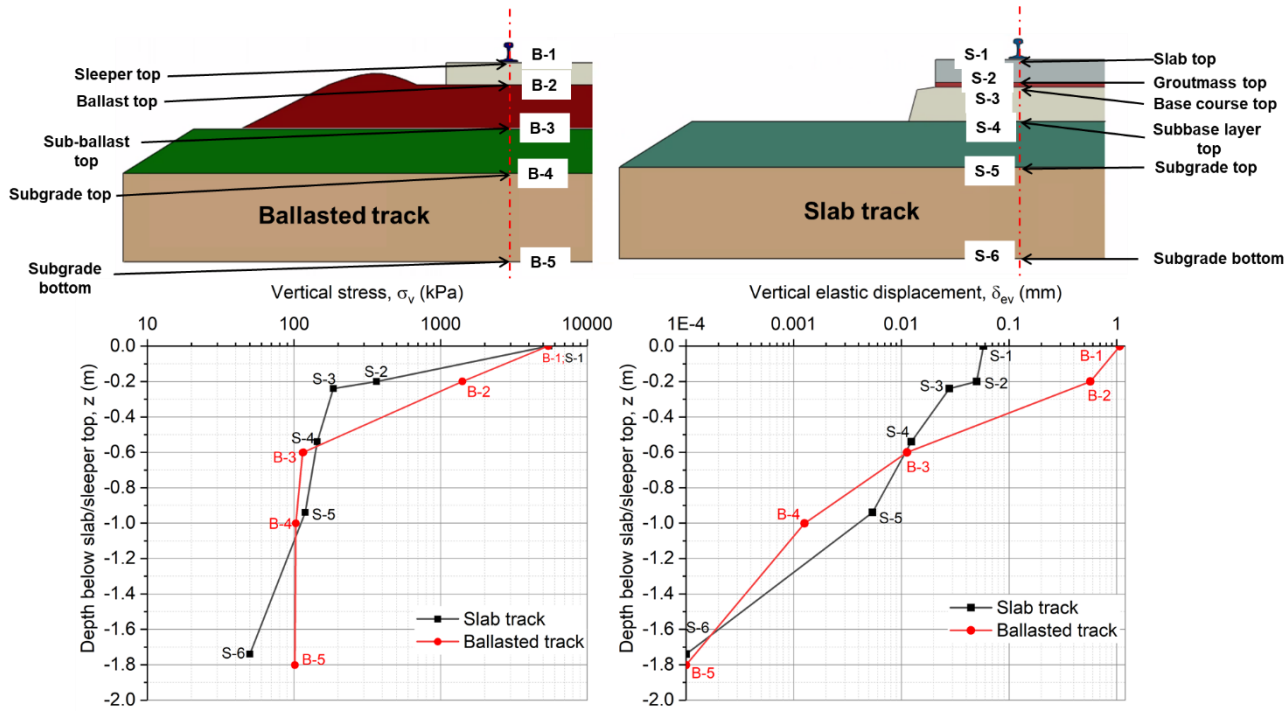

Figure 2. Distribution of vertical stress and vertical elastic displacement of various components of a slab track and ballasted track.

4. Model calibration for TDA

The uniaxial compression test was simulated in ABAQUS, replicating the dimensions of the compression equipment used by Meles et al. (2013), as shown in Figure 3. A uniform pressure of 200 kPa is applied at the top of the compression cell containing TDA. The simulated density state of the TDA is dense with a unit weight of 6.5 kN/m^3, which is the typical value of the field-compacted unit weight of TDA (Meles et al., 2013). The experimental stress-strain behaviour of TDA measured by Meles et al. (2013) is input as uniaxial test data in the hyperelastic constitutive model available in ABAQUS. However, it is essential to adopt a proper strain energy potential function. Hence, stability analysis is performed for various strain energy potential functions, and coefficients are obtained. Trials were conducted with the coefficients of all the stable strain energy potential functions, that is Ogden (N = 1, 2, and 3), reduced polynomial (N = 1, 2, 3), and Arruda-Boyce. The stress-strain behaviour for each strain energy potential function is compared with the experimental result of Meles et al. (2013), as illustrated in Figure 4. Stress-strain output considering TDA as an elastic material has also been

examined in Figure 4. It is apparent that TDA cannot be modelled as an elastic material. It can also be observed from Figure 4 that reduced polynomial strain energy potential functions with $N \geq 2$ show better match with Meles et al. (2013). Among these, Yeoh (reduced polynomial with N = 3) has been adopted for the study as there was no difference in the computational effort for N = 2 and N = 3 and slightly better accuracy is observed for N = 3. The coefficient values of the Yeoh strain energy potential function, which have been used in the present study; viz. D_1, D_2, D_3, C_{10},C_{20}, and C_{30} are 7.02×10^{-6}, 0, 0, 73493.01, 177270.1, and 241047.72, respectively. The basic equations (equations A-8 to A-16) related to hyperelastic model are given in Appendix.

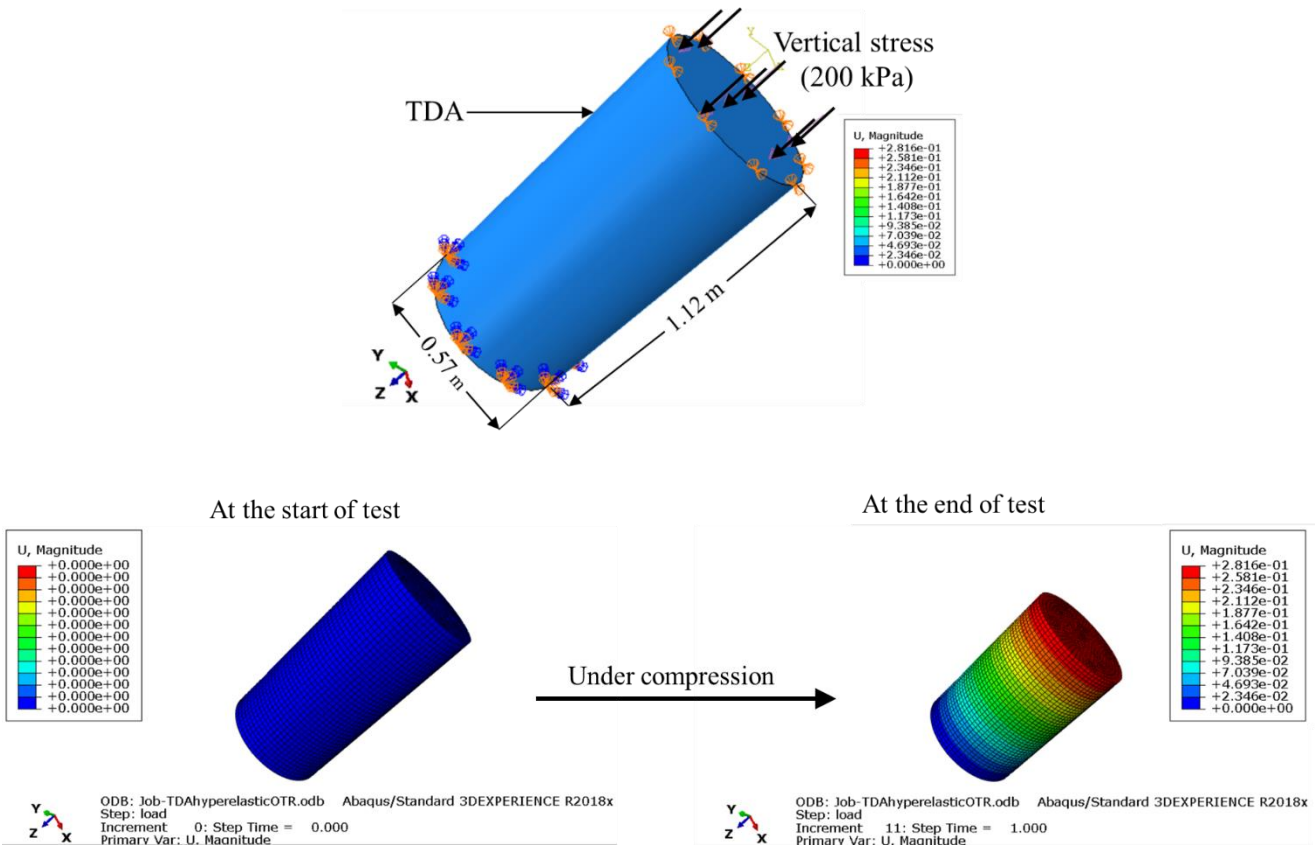

Figure 3. 3-D model of uniaxial compression test of TDA in ABAQUS.

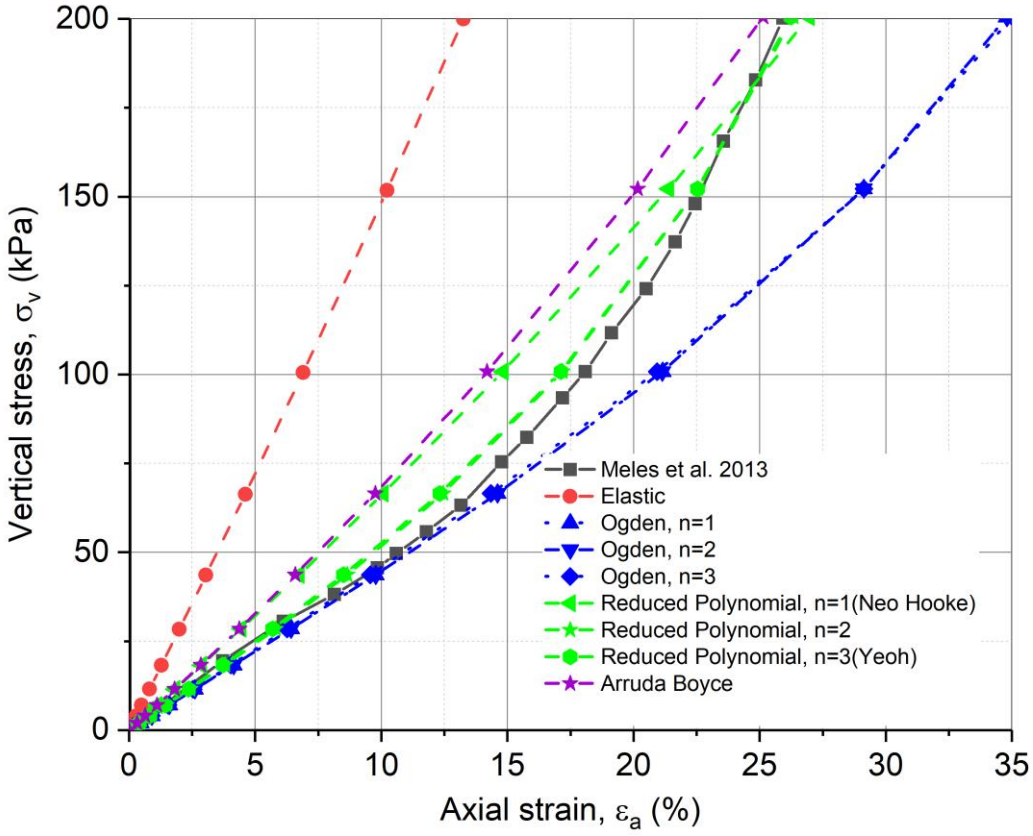

Figure 4. Stress-strain behaviour of various constitutive models for TDA

5. Effect of constitutive model selection for TDA

The adoption of the most suitable constitutive model for TDA is essential to accurately analyse the behaviour of TDA embedded track. It has been shown in Figure 4 that the hyperelastic constitutive model with the strain energy potential of at least two degree shows a good match with experimental data. Figures 5 (a) & (b) show the variation of vertical elastic displacement with load cycles when 25 mm TDA is placed below the base layer of slab track and subbase layer of a ballasted track, respectively. The trend here is shown only for ten load cycles for comparison of vertical elastic displacement in a slab track and ballasted track, when elastic and hyperelastic constitutive model is used for TDA in numerical analysis. It can be observed from Figure 5(a) that for a slab track, the vertical elastic displacement (δ_{ev}) and vertical plastic displacement or settlement (δ_{pv} or S_n) are underestimated by 59.2% and 42.4%, respectively when considering elastic constitutive behaviour for TDA. Similarly, for ballasted track, the

vertical elastic displacement and settlement are underestimated by 43.5% and 30.4%, respectively, for the elastic constitutive model compared to the hyperelastic constitutive model. Therefore, the selection of elastic behaviour of TDA for numerical modelling would lead to inaccurate assessment of stress and strains below TDA embedded track.

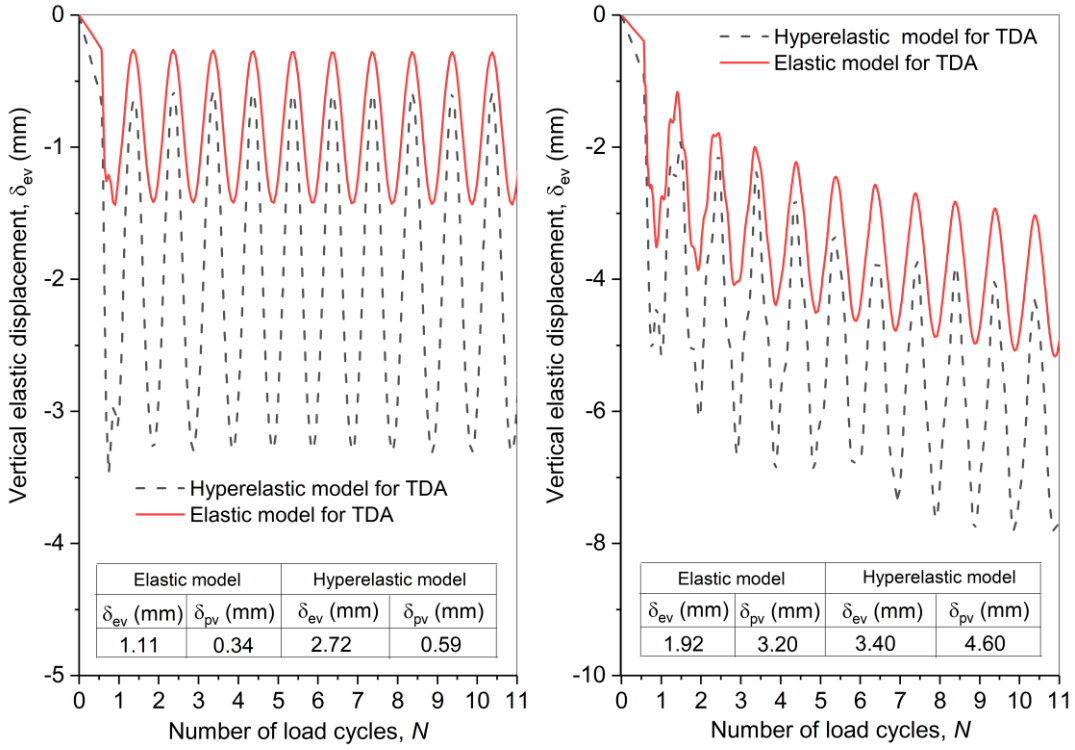

(a) (b)

Figure 5. Variation of vertical elastic displacement with load cycles for (a) slab track, (b) ballasted track, employing hyperelastic and elastic constitutive model for TDA.

6. Optimum location of TDA placement

The optimum location for placement of TDA in a ballasted and slab track is determined by placing the TDA layer of varying thickness at various locations, such as below groutmass. The model of a slab track is used to conduct a series of simulations with varying TDA thickness (0, 10 mm, 25 mm, 50 mm, and 100 mm) placed below groutmass, base layer, and subbase layer, as shown in Figure 6. A similar analysis is performed for a ballasted track with TDA in different thickness located below sleeper, ballast, and subballast, shown in Figure 6. Simulations are performed for 100 cycles at 5.6 Hz frequency (equivalent to train speed of 360 km/h).

The displacement limit in case of a slab track is 2.5 mm in Japanese HSR and 2 mm in Chinese HSR (Hu et al., 2018; Zhou, 1995). On the other hand, the displacement limit for a ballasted track is 9 mm for a track of light construction (Hay, 1982). Considering the above limits on displacement, the maximum allowable thickness of TDA when it is located below various components of a slab track and the ballasted track is obtained. As shown in Figure 7, the TDA thickness corresponding to displacement limit of 2.5 mm in a slab track is 15 mm, 25 mm, and 35 mm for TDA placed below groutmass, base layer, and subbase layer, respectively. The settlement corresponding to these TDA thickness is 0.3 mm, 0.6 mm, and 1.5 mm, respectively. Similarly, for a ballasted track (Figure 8), the maximum permissible TDA thickness is 35 mm, 50 mm, and 70 mm for TDA located below sleeper, ballast, and subballast, respectively. The corresponding settlement is 11.5 mm, 25 mm, and 12.5 mm for TDA located below sleeper, ballast, and subballast, respectively.

In case of a slab track, it is observed that for a particular TDA thickness, although least vertical elastic displacement is shown for TDA placed below the subbase layer, the settlement is maximum. For example, the vertical elastic displacement reduces by 50% for TDA placed below the subbase layer as compared to the case when TDA is placed below groutmass but settlement increases by a factor of 2.5. Considering this, TDA placed below the base layer provides a balance between vertical elastic displacement and settlement. Hence, the most suitable location for placement of TDA in a slab track is below the base layer (see Figure 7). In case of a ballasted track, it can be observed that the placement of TDA below subballast results in the least vertical elastic displacement and settlement, hence it is the most suitable location for its placement (see Figure 8). The reason for higher elastic displacement and settlement in the ballast layer compared to the base layer of slab track is due to higher stresses in ballast.

Using Fast Fourier Transform (FFT), the peak acceleration of concrete slab of the slab track and sleeper of the ballasted track is evaluated with and without TDA. It is evident from

Figure 9 that peak acceleration reduces by 50% and 42% on introducing 25 mm TDA below the base layer of slab track and below subballast layer, respectively. These reduced peak accelerations can be interpreted as the lowered vibration levels of slab track and ballasted track due to TDA incorporation.

The numerical analysis involving a large number of load cycles is computationally very expensive. Therefore, simulations of cyclic loading for a slab track and ballasted track with 25 mm TDA below base layer and subballast, respectively, is performed for 1000 load cycles. Figure 10 illustrates the variation of settlement with load cycles for the concrete slab of a slab track, with 25 mm TDA placed below the base layer. Equation (1) was primarily developed by Indraratna and Nimbalkar (2013) to compute settlement of granular materials; however, this equation was not proved good fit for track with TDA. A new equation [equation (2)] was therefore proposed which provided a very good match with a R^2 value of 0.97. Hence equation (2) was used to predict the settlement for both track types with TDA

$$S_n = S_1[1 + a \times \ln(N) + 0.5 \times b \times \{\ln(N))\}^2] \quad (1)$$

where S_1 and S_n are the settlement at the end of the 1st and nth cycle, respectively; a and b are empirical coefficients; N is the load cycle number.

$$S_n = S_1\{a + b \times \ln(N)\} \quad (2)$$

where S_1 and S_n are the settlement at the end of the 1st and nth cycle, respectively; a and b are empirical coefficients; N is the load cycle number.

Similarly, equation (2) is used for curve fitting and to predict settlement for 1 million cycles when 25 mm TDA is placed below subballast of a ballasted track. The derived empirical coefficients for slab track and ballasted track are shown in Figures 10 and 11, respectively.

A simple approach is developed to predict settlement for 1 million load cycles. Settlement prediction factor (*spf*), which is the ratio of settlement at the end of 1 million load

cycle to the settlement at the end of 100th load cycle, has been obtained for both track types, with and without TDA layer. The *spf* is calculated using equation (3).

$$spf = \frac{S_{1\times10^6}}{S_{100}} \tag{3}$$

where $S_{1\times10^6}$ and S_{100} are the settlement at the end of the 1 million and 100th load cycle, respectively.

In the parametric studies, the settlement for 1 million load cycles is predicted by multiplying the settlement at 100th load cycle with the values of *spf* for slab track and ballasted track, with and without TDA. For instance, it can be observed from Figure 10 that the settlement at 100th load cycles is 83% of settlement at the end of 1 million load cycles, demonstrating that the simulation performed for 100 load cycles represent a significant amount of long-term behaviour of TDA incorporated slab track. Hence, *spf* is 1.2 (1/0.83), and this *spf* is used to predict settlement (at the end of 1 million load cycles) for slab track embedded with 25 mm TDA below base layer. Similarly from Figure 11, in case of ballasted track with 25 mm TDA below subballast, the *spf* comes out to be 2.5 and this *spf* is used to predict settlement (at the end of 1 million load cycles) for ballasted track embedded with 25 mm TDA below subballast.

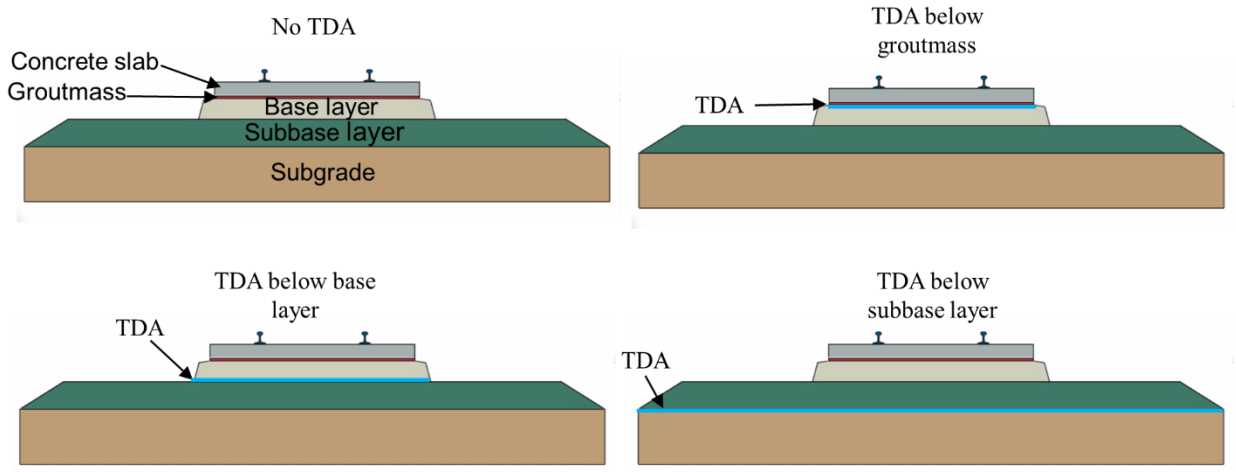

(a)

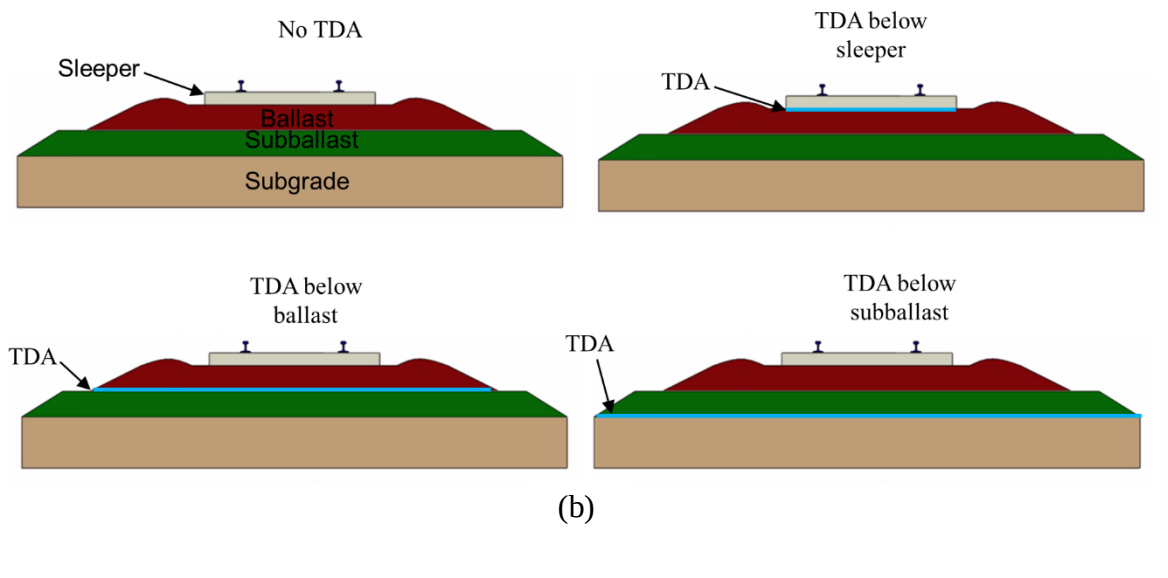

Figure 6. Geometry showing location of TDA below different components of (a) slab track (b) ballasted track used in the study.

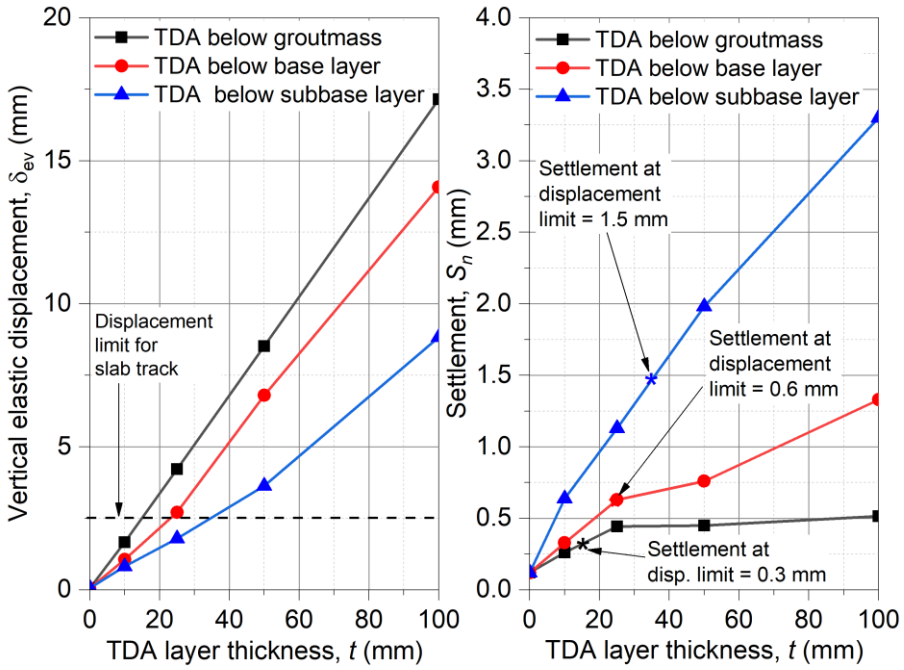

Figure 7. Variation of (a) vertical elastic displacement and (b) settlement with TDA thickness for a slab track at train speed of 360 km/h

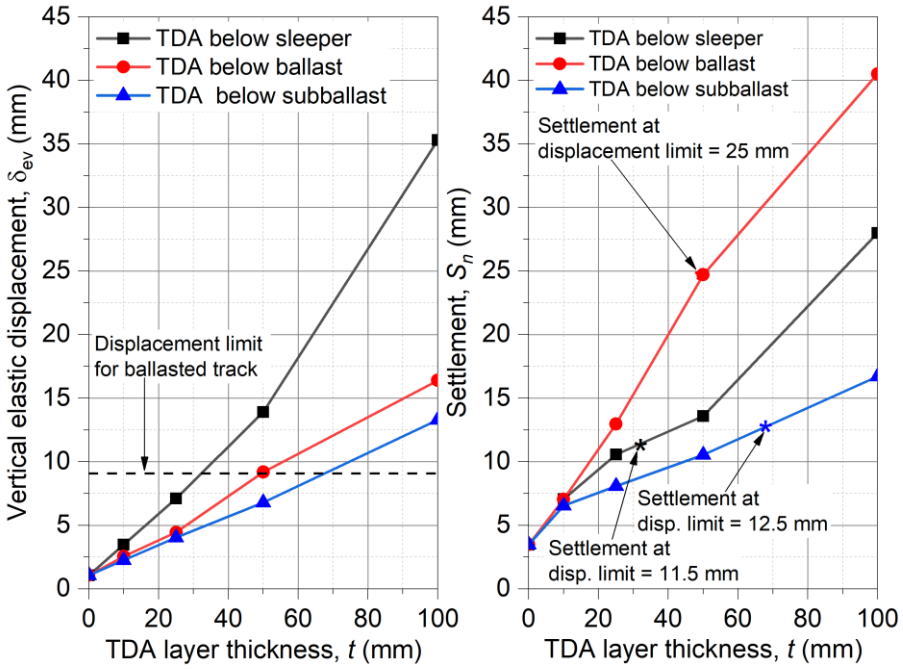

(a) (b)

Figure 8. Variation of (a) vertical elastic displacement and (b) settlement with TDA thickness for a ballasted track at train speed of 360 km/h

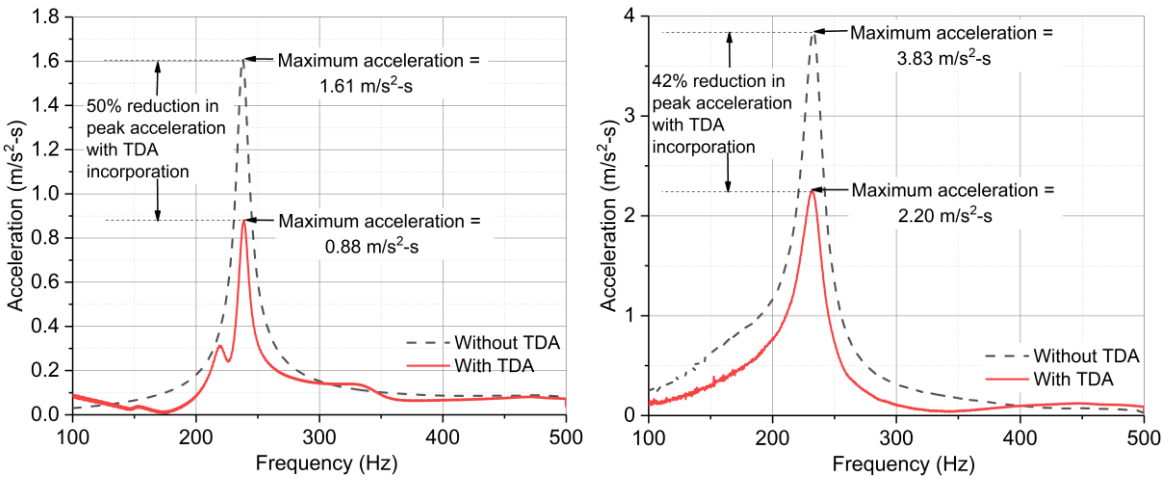

(a) (b)

Figure 9. Comparison of peak acceleration for (a) slab track (b) ballasted track, without TDA and with 25 mm TDA below base and subballast layer of slab track and ballasted track, respectively.

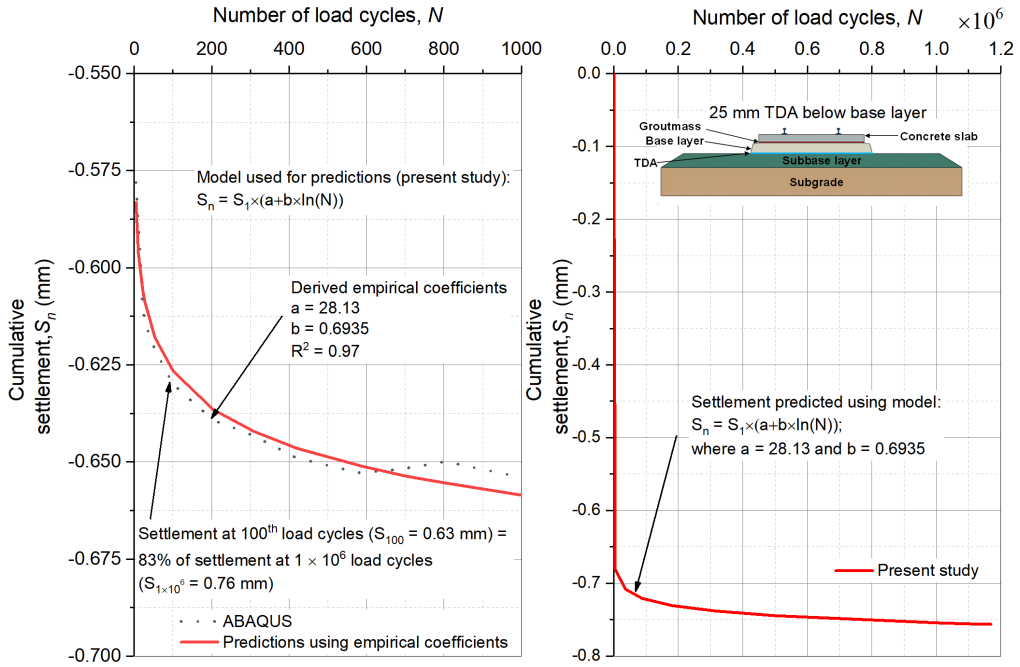

(a) (b)

Figure 10. (a) Empirical coefficient predictions for the slab track model (with 25 mm TDA placed below base layer) fitted against ABAQUS (b) prediction of settlement for 1.2 million load cycles.

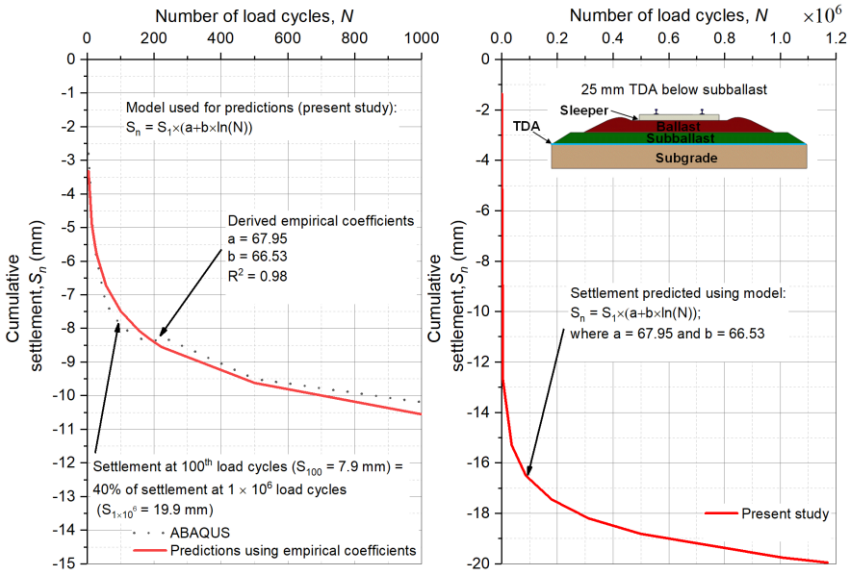

(a) (b)

Figure 11. (a) Empirical coefficient predictions for the ballasted track model (with 25 mm TDA placed below subballast) fitted against ABAQUS (b) prediction of settlement for 1.2 million load cycles.

7. Validation for slab track and ballasted track

The 3-D models of the slab track and ballasted track developed in ABAQUS were validated against the experimental results of Cebasek et al. (2018). Figure 12 illustrates that the predicted vertical displacement for rail and concrete slab during static loading show a good match with results reported by Cebasek et al. (2018). Vertical displacement versus time plot is obtained considering static loading in two steps: a) step one – application of 63.77 kN for 620 s; and b) step two – application of 83.34 kN for 788 s on the middle sleeper. The redistribution of load per actuator in the first step is 15.94 kN, 31.88 kN, and 15.94 kN and in the second step is 20.84 kN, 41.69 kN, and 20.84 kN, for the three actuators, respectively.

Figure 14 shows the vertical elastic displacement versus time plot based on axle load of 117.72 kN acting on the middle sleeper with a cyclic frequency of 5.6 Hz, which represents a train speed of 360 km/h based on bogie spacing. A load of 58.86 kN is applied on each actuator with a time interval of 0.0065 seconds between sleepers. Further details on loading arrangements and test setup can be found in Cebasek et al. (2018). The modelling of cyclic loading and simulating moving train load for 1.2 million load cycles is a computationally expensive task. Therefore, in this study, the FEM predictions for 1000 load cycles are compared with the empirical models [equation (1)] developed by Indraratna and Nimbalkar (2013), and these are found to be in a good agreement. The proposed empirical models can be used to predict track behaviour for a large number of load cycles as they follow the trends of FEM predictions reported in this study. The cumulative settlement for 1000 cycles is shown in Figure 13. The vertical elastic displacement and settlement values show a good match with the values reported by Cebasek et al. (2018), as shown in Figure 14 and Figure 15, respectively.

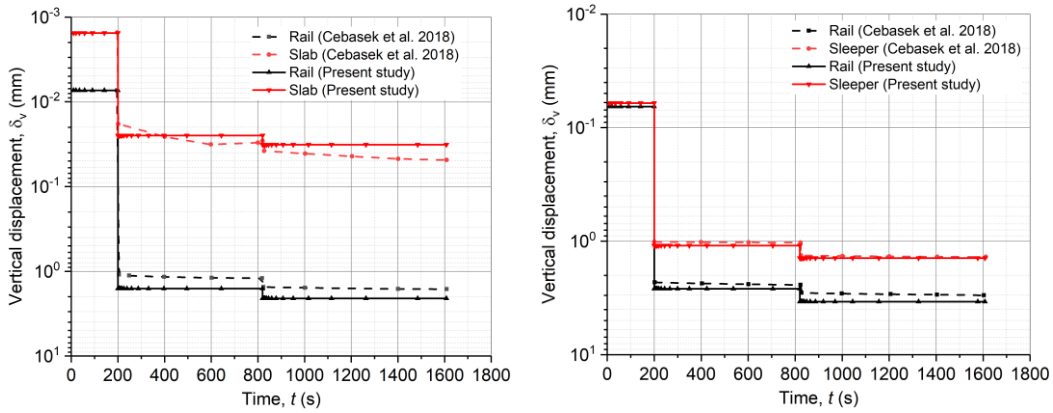

(a) (b)

Figure 12. Model validation for static loading with the experimental work of Cebasaek et al. 2018 for (a) slab track (b) ballasted track.

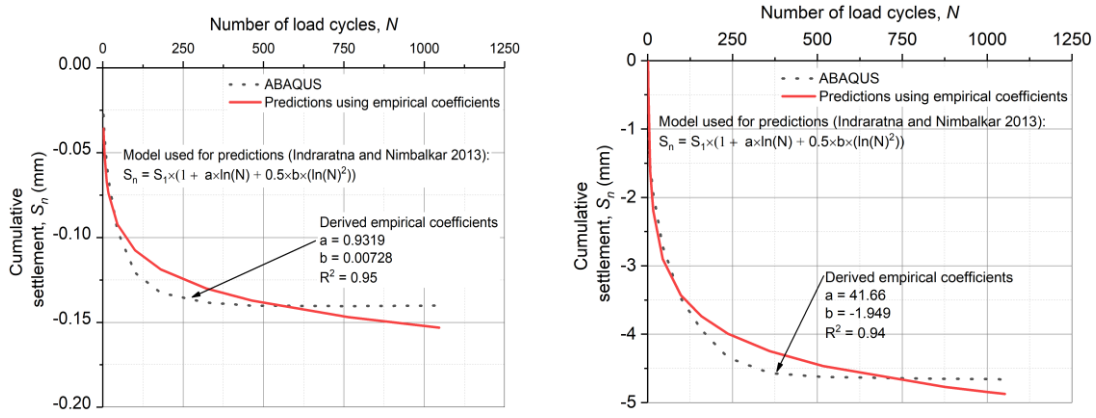

(a) (b)

Figure 13. Empirical coefficient predictions for the model fitted against ABAQUS output for (a) slab track (b) ballasted track.

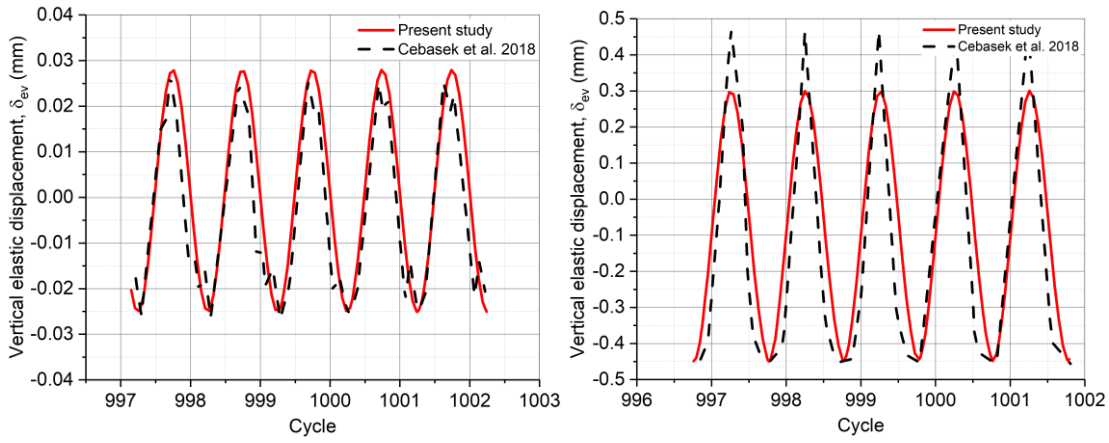

(a) (b)

Figure 14. Model validation against the experimental results reported by Cebasek et al. (2018) for vertical elastic displacement vs. cycle for (a) slab track, (b) ballasted track.

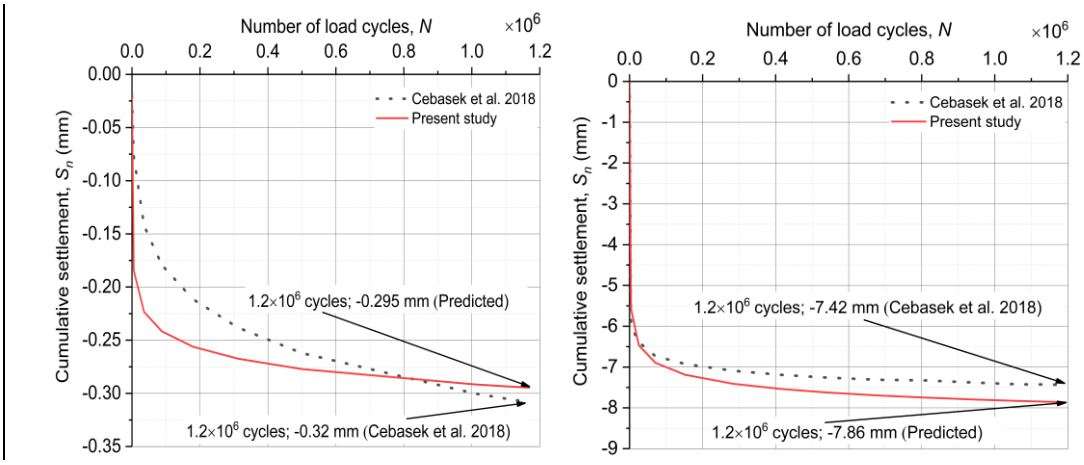

(a) (b)

Figure 15. Model validation against the experimental results reported by Cebasek et al. (2018) for cumulative settlement vs. the number of cycles for (a) slab track, (b) ballasted track.

8. Parametric study

A parametric study has been conducted to investigate the influence of train speed and axle load on the displacement (elastic and plastic) and stress response of both slab track and ballasted track, with and without TDA. For each analysis, only one parameter (train speed or axle load) is changed at an instant while others are kept constant. All the simulations are performed for the case when a 25 mm thick TDA layer is provided below the base layer and subballast layer

of slab track and ballasted track, respectively. All the simulations are performed for 100 load cycles, and then settlement is predicted for 1 million load cycles based on the methodology explained in the previous section and using equations (2–3).

7.1 Effect of train speed

The train speeds considered in this study are 160 km/h, 260 km/h, 360 km/h, and 450 km/h, which represent a loading frequency of 2.5 Hz, 4 Hz, 5.6Hz, and 7 Hz, respectively. The frequency of each train speed is calculated using either equation (4a) or equation (4b).

$$f = \frac{v}{\lambda} \tag{4a}$$

$$f' = \frac{V}{3.6 \times \lambda} \tag{4b}$$

where v and V are the train speeds in m/s and km/h, respectively; f or f' is the frequency in Hz; λ is the vehicle geometry (or wavelength) in m, which is categorised into three types: λ_a as the axle spacing, λ_b as the bogie spacing, and λ_v as the vehicle length [refer Figure 16(a)].

This vehicle geometry for computation of frequency can be vehicle length, bogie spacing or axle spacing (Milne et al., 2017), as shown in Figure 16(a). Past studies have used vehicle passing frequency (Milne et al., 2017), bogie passing frequency (Cebasek et al., 2018), and axle passing frequency (Indraratna and Nimbalkar, 2013) in their research.

The axle passing frequency (f_a *or* f_a'), bogie passing frequency (f_b *or* f_b'), and vehicle passing frequency (f_v *or* f_v') are represented by equations (5), (6), and (7), respectively.

$$f_a = \frac{v}{\lambda_a} \tag{5a}$$

$$f_a' = \frac{V}{3.6 \times \lambda_a} \tag{5b}$$

$$f_b = \frac{v}{\lambda_b} \tag{6a}$$

$$f_b' = \frac{V}{3.6 \times \lambda_b} \tag{6b}$$

$$f_v = \frac{v}{\lambda_v} \tag{7a}$$

$$f_v' = \frac{V}{3.6 \times \lambda_v} \tag{7b}$$

In the present study, train speed is based on bogie passing frequency and different train speeds are obtained by varying loading frequency as shown in Figure 16(b). For instance, based on bogie spacing of 18 m, the bogie passing frequency for a train travelling at 100 m/s or 360 km/h can be calculated as 5.6 Hz using equation 6(a) or 6(b), respectively.

Figures 17 and Figure 18 show the variation of vertical elastic displacement and settlement for a slab track and ballasted track, respectively. The vertical elastic displacement and settlement values have been reported at the end of 1 million load cycles, and correspond to a concrete slab (top) and sleeper (top) for a slab track and ballasted track, respectively. It can be seen that without TDA, vertical elastic displacement decreases with the increase of train speed in both the tracks. However, on addition of TDA layer, the vertical elastic displacement increases with increasing train speeds in a slab track and shows a fluctuating trend in a ballasted track. In the slab track, the settlement decreases with an increase in train speed for both conditions (that is, with and without TDA). The settlement in a ballasted track without TDA reduces with an increase in train speed. However, with TDA the settlement in ballasted track, increases for train speed up to 250 km/h, reduces for train speed up to 350 km/h, and then increases again. One important thing to note is that in a slab track, settlement decreases with train speed while it shows fluctuating trend with train speed in a ballasted track. This highlights the significance of slab track in showing better performance in terms of reduced settlement for high-speed trains, both with and without rubber layer.

Generally, it can be observed in Figure 18 that both the vertical elastic displacement and settlement show a fluctuating trend with TDA incorporation in a ballasted track. The maximum settlement for slab track embedded with TDA below base layer at the end of 1

million load cycle is approximately 0.88 mm and 0.38 mm at train speed of 160 km/h and 450 km/h, respectively. Similarly, the settlement in a ballasted track embedded with TDA below the base layer is approximately 18.4 mm and 23.25 mm at train speed of 160 km/h and 450 km/h, respectively. It is important to consider long-term performance of railway track which is illustrated by the fact that settlement reported for few load cycles are not representative of the actual behaviour of the railway track. For instance, at low train speeds settlement of ballasted track with 25 mm TDA below subballast at 100^{th} load cycle is 7.4 mm, which is below the vertical displacement limit of 9 mm (Hay, 1982). However, settlement for the same ballasted track at the end of 1 million load cycles is 18.4 mm, exceeding the vertical displacement limit of 9 mm, even at low train speeds. On the contrary, the maximum settlement for a slab track is 0.88 mm, which is well below the displacement limit of 2.5 mm (Hu et al., 2018; Zhou, 1995). Besides, the use of TDA as a layer is more suitable for a slab track compared to ballasted track as the maximum displacement is within specified limits for slab tracks.

Figures 19 (a) & (b) show the variation of horizontal elastic displacement with train speed for a slab track and ballasted track, respectively. It can be seen that horizontal displacement increases and decreases with increasing train speeds in a slab track and ballasted track, respectively. The peak horizontal displacement is less than 1 % of the peak vertical displacement for both ballasted and slab track.

Figures 20 and 21 illustrate the vertical and horizontal stress contour, respectively for a slab track with varying depth and train speed. It can be observed that train speed has the least impact on the vertical stress at various depths in a slab track below the concrete slab but influences the horizontal stress at depths greater than 0.4 m below concrete slab top. The incorporation of TDA reduces the vertical and horizontal stress level at depths greater than 0.4 m in a slab track, for varying train speed. For instance, the vertical stress reduces from 200 kPa to around 100 kPa within 0.2 m depth of TDA placement. The addition of TDA also eliminates the influence of train speed on the fluctuating horizontal stress in a slab track. Figures 22 and

23 show the vertical and horizontal stress contour, respectively for a ballasted track with varying depth and train speed. As can be seen from the figures the train speed has negligible influence on the horizontal and vertical stresses. However, the effect of train speed on the vertical and horizontal stress levels becomes noticeable for the lower layers of the ballasted track after TDA incorporation. With TDA incorporation, the vertical stress levels at depth greater than 0.9 m below sleeper top, reduce by approximately 33% but the horizontal stress levels remains the same. The above discussion demonstrates the effectiveness of TDA in reducing both vertical and horizontal stresses in a slab track but only vertical stress reduction in a ballasted track.

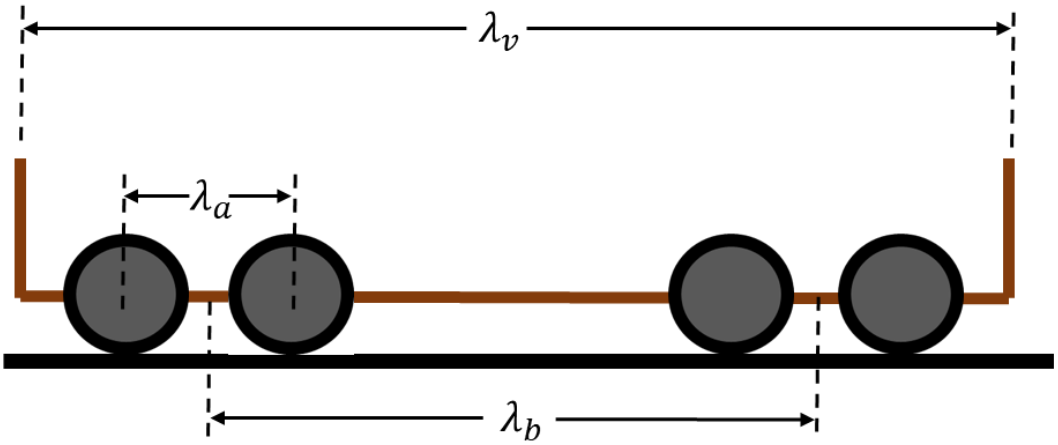

Figure 16(a). Typical vehicle geometry, λ_a is the axle spacing, λ_b is the bogie spacing, and λ_v is the vehicle length.

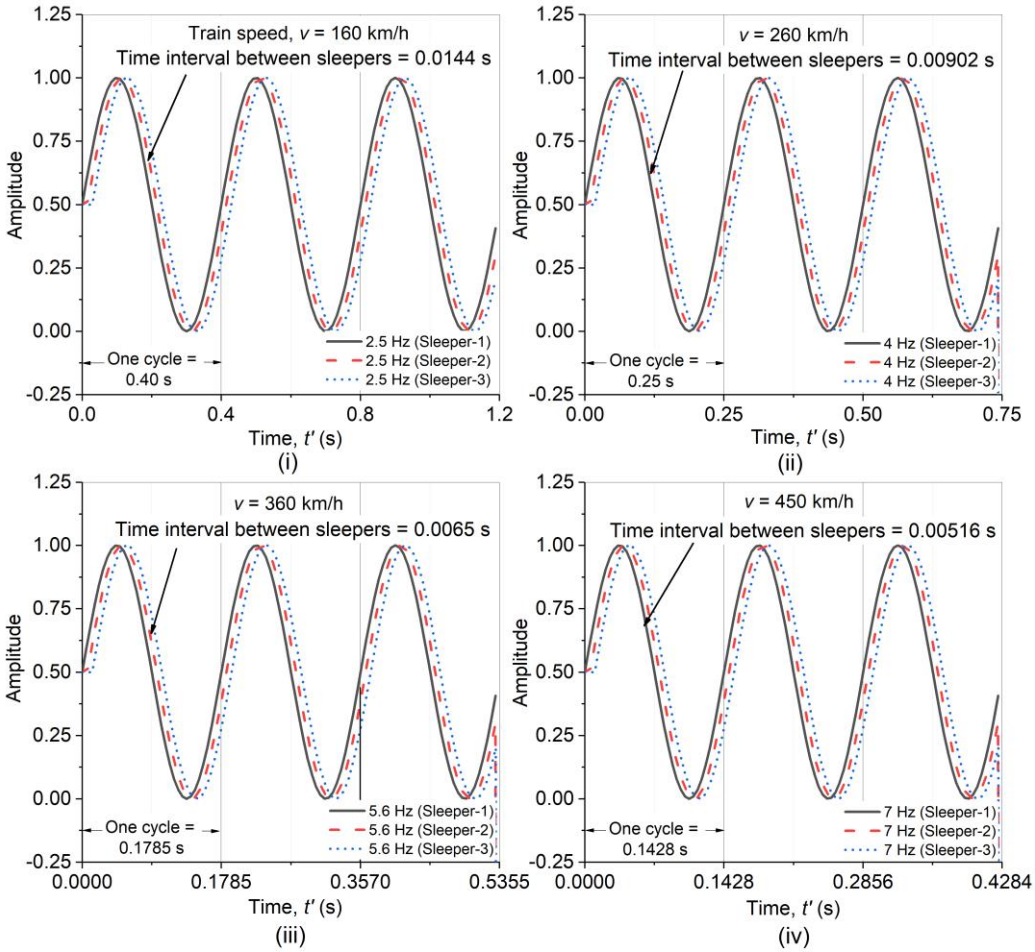

Figure 16(b). Variation of amplitude with time, simulating train speeds of approximately 160 km/h, 260 km/h, 360 km/h, and 450 km/h by using loading frequency of (i) 2.5 Hz, (ii) 4 Hz, (iii) 5.6 Hz, and (iv) 7 Hz respectively, based on bogie spacing of 18 m.

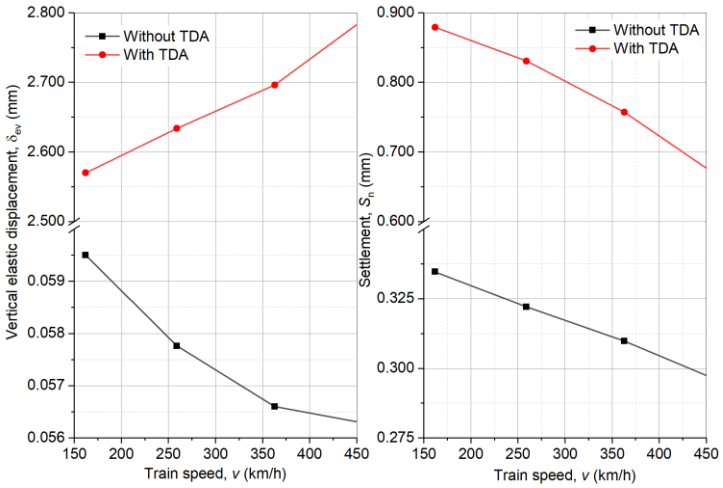

Figure 17. Variation of (a) vertical elastic displacement and (b) settlement with train speed, with and without 25 mm TDA below base course in a slab track.

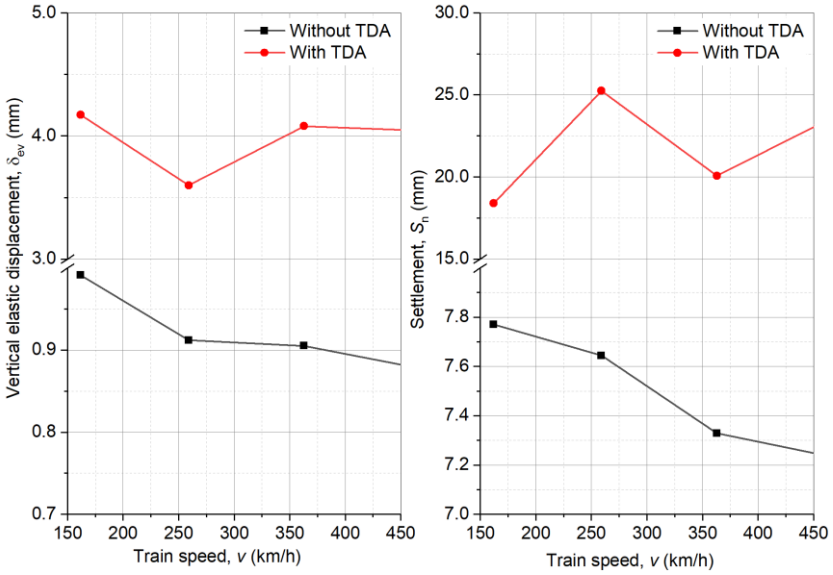

(a) (b)

Figure 18. Variation of (a) vertical elastic displacement and (b) settlement with train speed, with and without 25 mm TDA below subballast in a ballasted track.

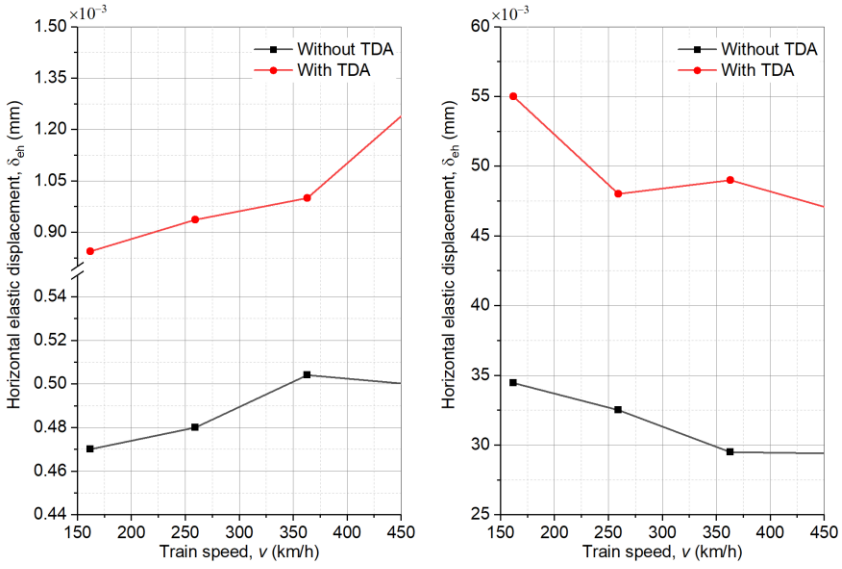

(a) (b)

Figure 19. Variation of horizontal elastic displacement with train speed for (a) slab track (b) ballasted track.

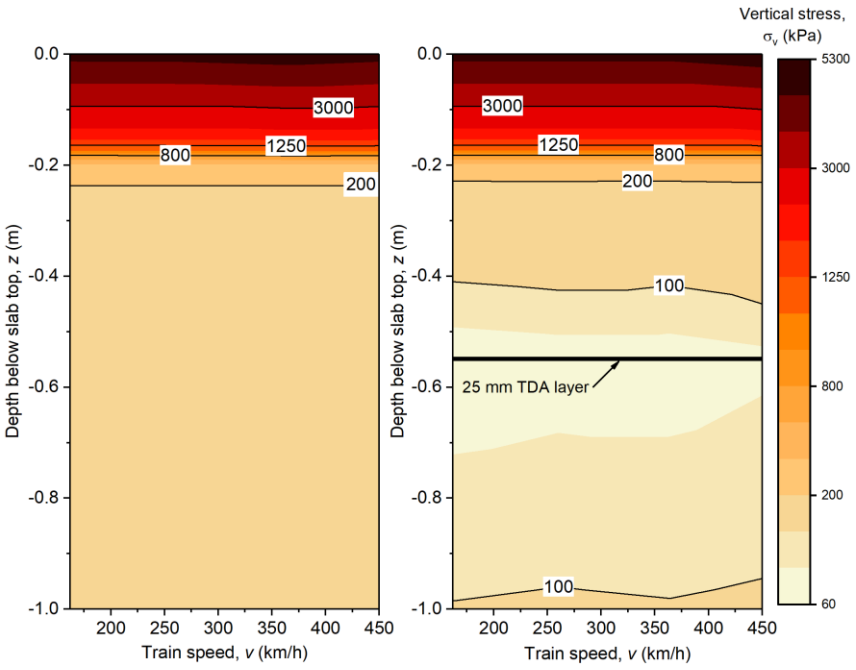

(a) (b)

Figure 20. Vertical stress contour for varying depth and train speed, (a) without TDA (b) with 25 mm TDA below the base layer, for a slab track.

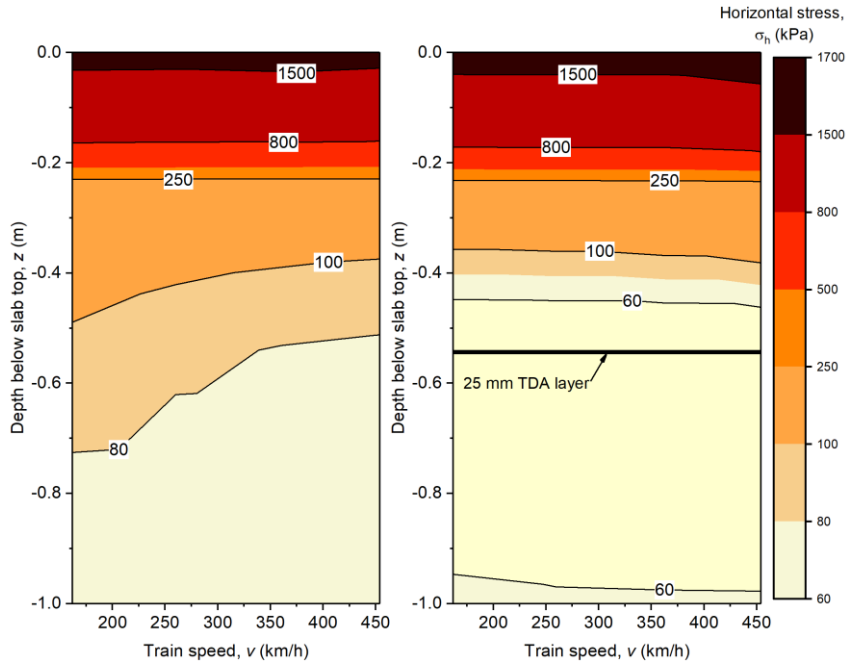

(a) (b)

Figure 21. Horizontal stress contour for varying depth and train speed, (a) without TDA (b) with 25 mm TDA below the base layer, for a slab track.

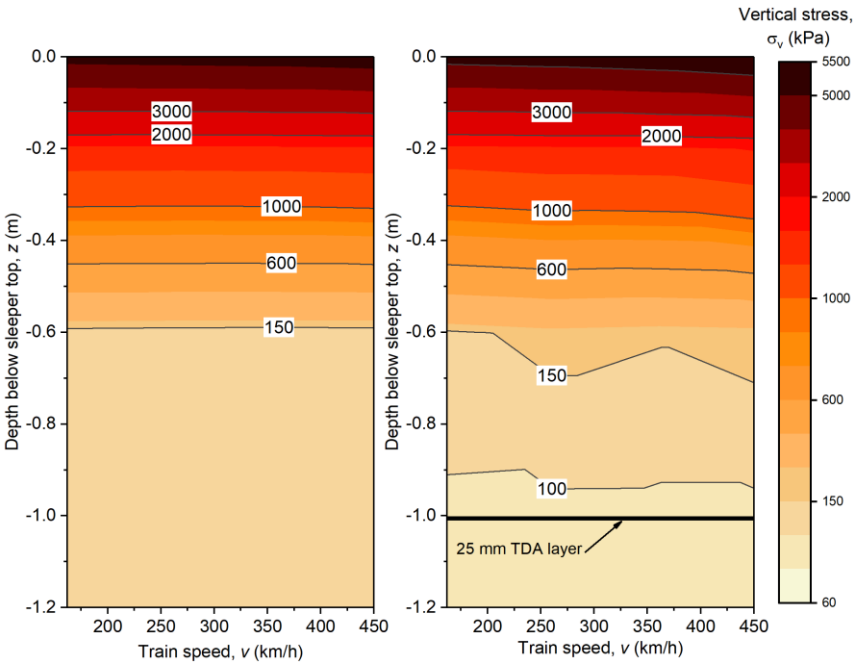

(a) (b)

Figure 22. Vertical stress contour for varying depth and train speed, (a) without TDA (b) with 25 mm TDA below the subbase layer, for a ballasted track.

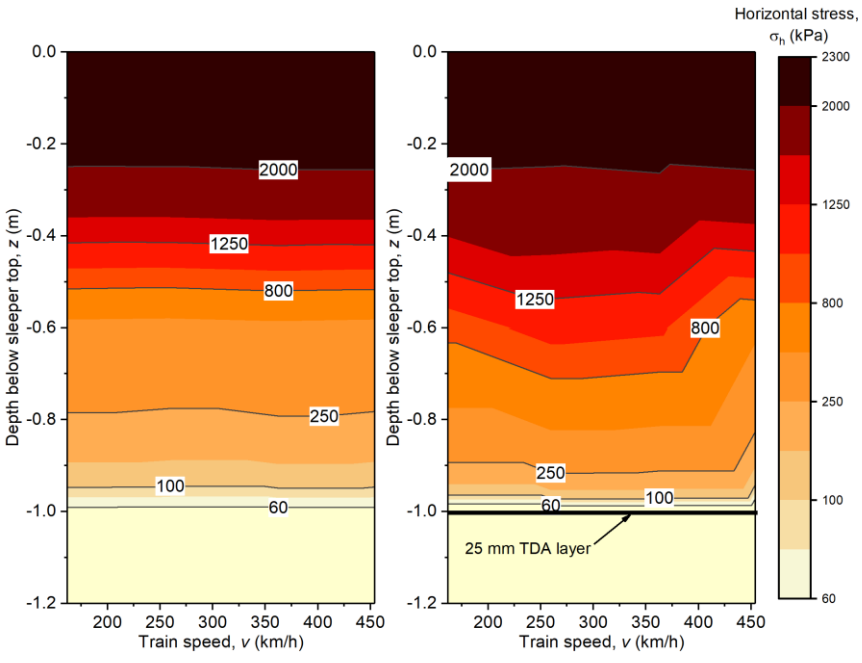

(a) (b)

Figure 23. Horizontal stress contour for varying depth and train speed, (a) without TDA (b) with 25 mm TDA below the subbase layer, for a ballasted track.

7.2 Effect of axle load

The axle loads considered in this study are 117.7 kN, 166.7 kN, 200 kN, and 230 kN which represent axle load of passenger trains of different countries. Figures 24 and 25 illustrate the variation of vertical elastic displacement and settlement for slab track and ballasted track, respectively with varying axle loads. It can be seen from Figure 24 that the vertical elastic displacement increases with an increase in axle load for slab track, with and without TDA. The settlement rises with an increase in axle loads for a slab track without TDA; however, the incorporation of TDA reduces the rate of settlement rise. The settlement of the slab track with TDA starts reducing for axle load higher than 200 kN. This shows the effectiveness of TDA in reducing settlement for a slab track at higher axle load.

It can be seen from Figure 25 that both vertical elastic displacement and settlement rises with an increase in axle load of the train. With TDA, even at lower axle load the vertical displacement limit is exceeded. Hence, the use of TDA is not recommended for a ballasted track.

Figures 26 (a) & (b) show the variation of the horizontal elastic displacement with axle load for a slab track and ballasted track, respectively. It can be seen that horizontal displacement increases with axle load in both track types. The horizontal displacement in a slab track increases with TDA incorporation, however, it remains the same for ballasted track both with and without for axle load of 160–205 kN. The horizontal displacement in a ballasted track for axle load higher than 205 kN gets reduced with incorporation of TDA.

Figures 27 and 28 illustrate the vertical and horizontal stress contour, respectively for a slab track with varying depth and axle load. Figures 29 and 30 illustrate the vertical and horizontal stress contours, respectively for a ballasted track with varying depth and axle load. It can be observed that the axle load has a significant effect on both vertical and horizontal stress at various depths in a slab track and ballasted track. The beneficial role of TDA in

reducing the vertical and horizontal stresses is apparent at a depth greater than 0.2 m and 0.4 m, respectively below concrete slab in a slab track for varying axle loads. The influence of TDA in reducing the vertical stress in a ballasted track is not observed but is noticeable for horizontal stress at depths greater than 1 m for all axle loads.

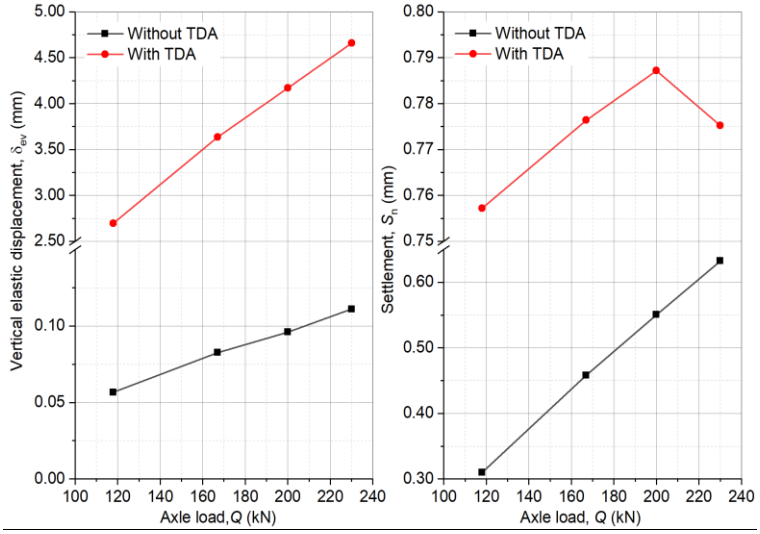

(a) (b)

Figure 24. Variation of (a) vertical elastic displacement and (b) settlement with axle load, with and without 25 mm TDA below the base layer in a slab track.

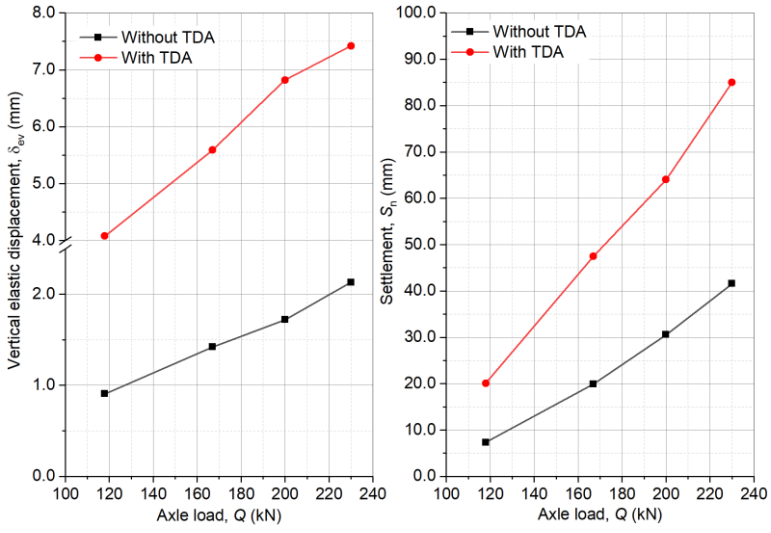

(a) (b)

Figure 25. Variation of (a) vertical elastic displacement and (b) settlement with axle load, with and without 25 mm TDA below subballast in a ballasted track.

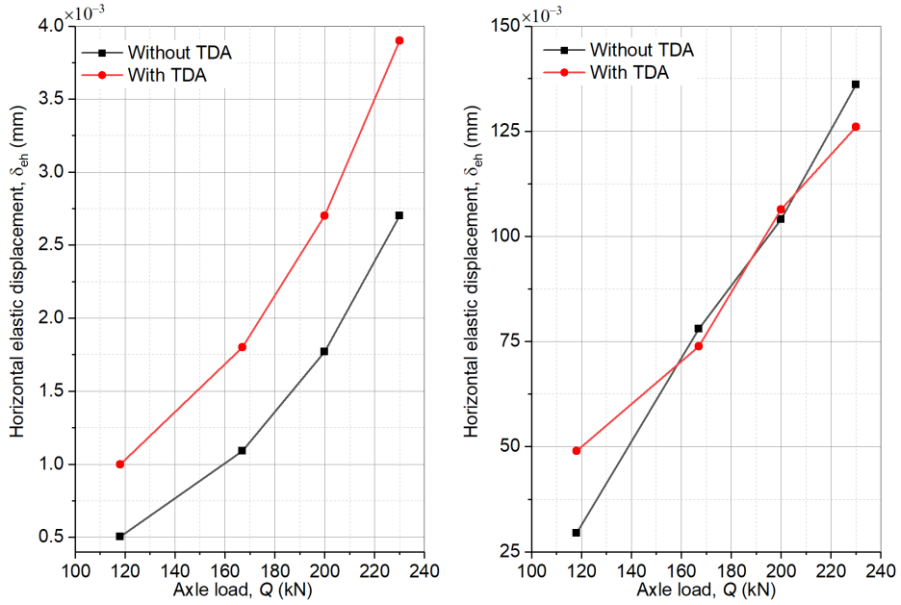

Figure 26. Variation of horizontal elastic displacement with axle load for (a) slab track (b) ballasted track.

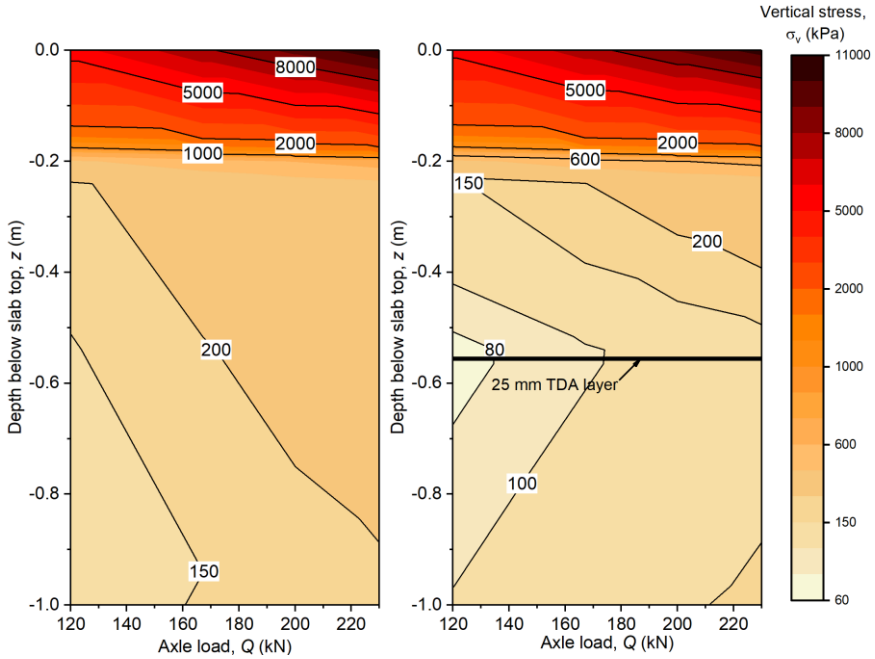

Figure 27. Vertical stress contour for varying depth and axle load for a slab track: (a) without TDA (b) with 25 mm TDA below the subbase layer.

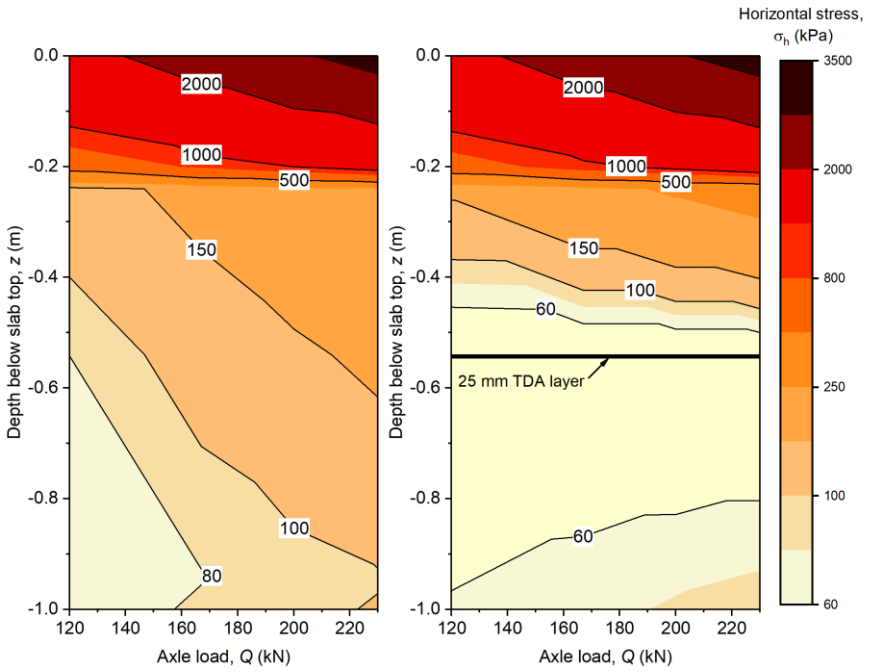

(a) (b)

Figure 28. Horizontal stress contour for varying depth and axle load for a slab track: (a) without TDA (b) with 25 mm TDA below the subbase layer.

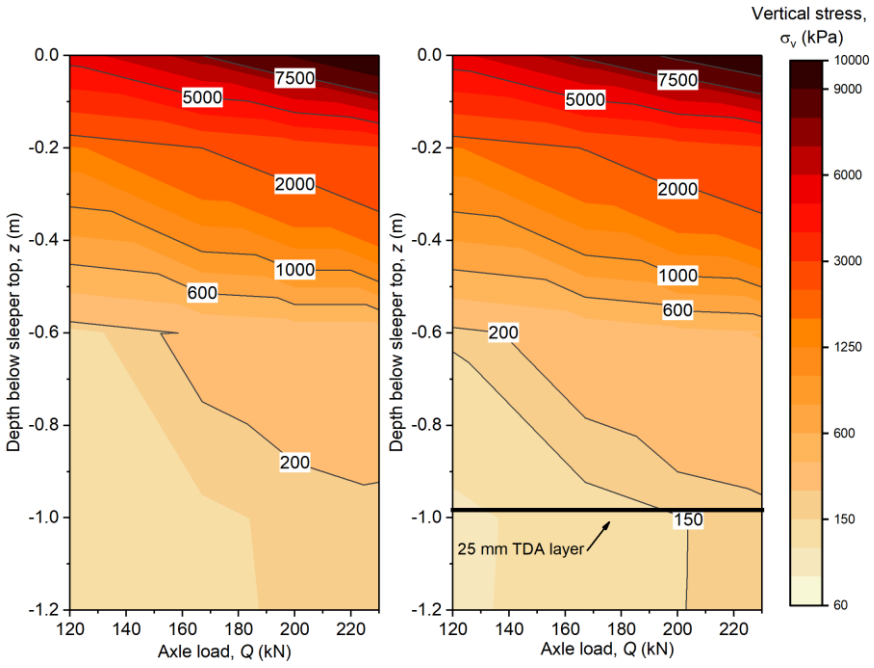

(a) (b)

Figure 29. Vertical stress contour for varying depth and axle load for a ballasted track: (a) without TDA (b) with 25 mm TDA below the subbase layer.

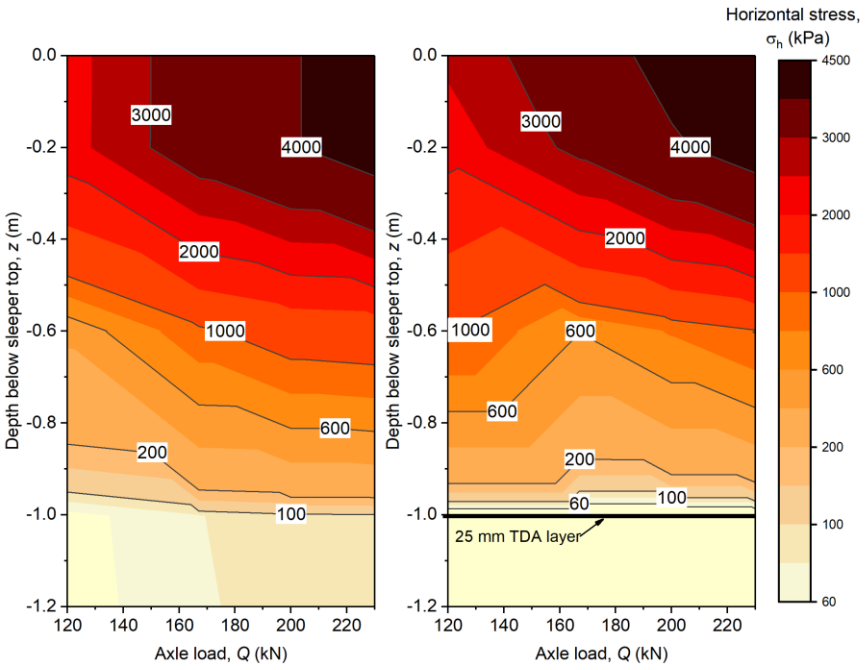

Figure 30. Horizontal stress contour for varying depth and axle load for a ballasted track: (a) without TDA (b) with 25 mm TDA below the subbase layer.

9. Limitation

One important aspect associated with finite element modelling when dealing with dynamic modelling is its size. The dynamic model should be large enough compared to static model to avoid disturbance occurring due to wave reflection at the boundary of the finite element mesh. Hence, specific care must be ensured in dealing with model boundaries to yield accurate responses (Kouroussis et al., 2011). Various solutions have been proposed by researchers to deal with wave reflections, such as the use of non-reflecting viscous boundaries (Lysmer and Kuhlemeyer, 1969), use of the infinite element method (Bettess, 1977), use of scaled boundary finite element method (Wolf and Song, 1996). Despite various solutions suggested by various researchers to deal with the issue of wave propagation, it is necessary to develop a larger model when dealing with the dynamic analysis of track. However, owing to this large mesh size, the computational cost of a dynamic finite element model is excessively high.

In the present study, due to a lab size track model, wave reflection can occur; however, material damping will reduce the intensity of wave reflections. Besides, TDA can also help in the attenuation of wave reflection. Moreover, as the main aim of the present study is the long-term performance comparison of TDA in a ballasted and slab track, a lab size track model is used. The computational cost of a full-size track model would have been very high to perform such analysis. The assumption of stationary load which is cyclically applied compared to moving load has further helped to simplify the numerical analysis. The effect of wave reflection has not been considered in the simulation. However, the authors were able to capture the performance of slab track and ballasted track in terms of vertical displacement under static and cyclic loading, and settlement as reported by Cebasek et al. (2018). In addition, similar model dimensions have been used by recent finite element studies by Ramos et al. (2021) to evaluate the influence of track foundation on the performance of ballasted and slab track and Sainz-Aja et al. (2020) to assess the dynamic behaviour of the trains and performance evaluation of track structure of a slab track.

10. Conclusion

A numerical study evaluating the long-term performance of ballasted and slab track incorporating TDA is presented in this paper. The constitutive model for TDA is determined and then used to investigate the effect of TDA on vibration and displacement response of both track types. The influence of train speed and axle load on the behaviour of slab track and ballasted track, with and without TDA is also investigated. The following conclusions can be drawn from this study:

- The adoption of the elastic constitutive model for TDA leads to an underestimation of strains at a particular stress level. The hyperelastic constitutive model with strain energy potential of at least degree 2 should be used for TDA.

- The TDA is effective in reducing the peak acceleration of both slab track and ballasted track, which relates to reduced vibration of the railway tracks. The peak acceleration reduced by 50% and 42% for slab track and ballasted track, respectively with TDA incorporation.
- TDA is effective in reducing vertical as well as horizontal stress in lower components of the slab track for varying train speeds and axle loads. However, only vertical stress reduction and only horizontal stress reduction was observed with the use of TDA in a ballasted track for varying train speeds and axle loads, respectively.
- The developed model [equation (2)] can predict settlement for ballasted and slab track with TDA. The settlement reported for a small number of load cycles is not representative of actual track performance.
- The influence of train speed on vertical displacement response is more noticeable in a slab track compared to ballasted track, both with and without TDA. TDA is effective in reducing settlement for higher axle load in a slab track compared to ballasted track. The influence of axle load on vertical displacement response is observed for both track forms. The horizontal elastic displacements are less than 1 % of the vertical elastic displacements in both ballasted and slab track.

Declaration of Competing Interest

None.

Acknowledgments

This work is a part of the first author's doctoral study. This research was financially supported by a UTS International Research Scholarship and UTS President's Scholarship. This support is gratefully acknowledged.

Notation

The following symbols are used in this paper:

a, b = empirical coefficients;

A_{i0}, A_{10}, A_{20}, A_{30}, B_i, B_1, B_2, B_3, μ_i, α_i, λ_m = temperature-dependent material parameters;

E= elastic modulus (N/m^2);

f *or* f', f_a *or* f_a', f_b *or* f_b', f_v *or* f_v' = frequency, axle passing frequency, bogie passing frequency, vehicle passing frequency, respectively (Hz);

G_0, G = initial shear modulus and shear modulus, respectively (N/m^2);

I'_1 = first invariant of the stress tensor (N/m^2);

$I'_{1,axi}$ = first invariant of the stress tensor for axisymmetric configuration (N/m^2);

$\bar{I}_1$ = first deviatoric strain invariant (%);

J, J^{el} = the total volume ratio and elastic volume ratio, respectively (%);

J_2 = second invariant of the deviatoric stress tensor (N/m^2);

$J_{2,axi}$ = second invariant of the deviatoric stress tensor for axisymmetric configuration (N/m^2);

K'_0 = effective bulk modulus (N/m^2);

n = material parameter;

N = number of load cycles;

Q = axle load (N);

S_1, S_{100}, $S_{1\times10^6}$, S_n = settlement at the end of 1st, 100th, 1 million, and nth load cycle, respectively;

t = TDA layer thickness (m);

t' = time (s);

U = strain energy per unit of reference volume (N/m^2);

α, β = material constants;

λ, λ_a, λ_b, λ_v = vehicle geometry (or wavelength), axle spacing, bogie spacing, vehicle length, respectively (m);

$\bar{\lambda}_i$, λ_i= deviatoric stretches and principal stretches, respectively;

σ_v , σ_h = vertical and horizontal stress, respectively (N/m^2);

σ'_1, σ'_2, σ'_3 = the principal effective stresses (N/m^2);

ε_a = axial strain (%);

τ_{oct}= octahedral shear stress (N/m^2);

$\tau_{oct,axi}$ = octahedral shear stress for axisymmetric configuration (N/m^2);

δ_{ev}, δ_{pv} = vertical elastic displacement and vertical plastic displacement (m);

ν = Poisson's ratio;

$\emptyset$ = friction angle (˚);

ψ = dilation angle (˚);

ζ = damping ratio (%);

ρ = mass density (kg/m^3);

References

Abadi, T., Le Pen, L., Zervos, A., Powrie, W., 2015. Measuring the area and number of ballast particle contacts at sleeper-ballast and ballast-subgrade interfaces. Int. J. Railw. Technol. 4, 45–72. https://doi.org/10.4203/ijrt.4.2.3

Abaqus Online Documentation, 2018. Abaqus analysis user's manual C Dassault systèmes [WWW Document]. Hibbit, Karlsson Sorensen Inc., RI, USA; URL https://abaqus-docs.mit.edu/2017/English/SIMACAEMATRefMap/simamat-c-hyperelastic.htm (accessed 10.1.20).

Alejano, L.R., Bobet, A., 2012. Drucker–Prager Criterion. Rock Mech. Rock Eng. 45, 995–999. https://doi.org/10.1007/s00603-012-0278-2

Alves Costa, P., Calçada, R., Silva Cardoso, A., 2012. Ballast mats for the reduction of railway traffic vibrations: Numerical study. Soil Dyn. Earthq. Eng. 42, 137–150. https://doi.org/10.1016/j.soildyn.2012.06.014

Asadi, M., Mahboubi, A., Thoeni, K., 2018. Discrete modeling of sand–tire mixture considering grain-scale deformability. Granul. Matter 20, 18. https://doi.org/10.1007/s10035-018-0791-4

Bettess, P., 1977. Infinite elements. Int. J. Numer. Methods Eng. 11, 53–64.

Bian, X., Jiang, H., Cheng, C., Chen, Y., Chen, R., Jiang, J., 2014. Full-scale model testing on a ballastless high-speed railway under simulated train moving loads. Soil Dyn. Earthq. Eng. 66, 368–384. https://doi.org/10.1016/j.soildyn.2014.08.003

BS EN 13674-1, 2011. Railway applications - Track - Rail Part 1: Vignole railway rails 46 kg/m and above. Br. Stand. Inst.

Cebasek, T.M., Esen, A.F., Woodward, P.K., Laghrouche, O., Connolly, D.P., 2018. Full scale laboratory testing of ballast and concrete slab tracks under phased cyclic loading. Transp. Geotech. 17, 33–40. https://doi.org/10.1016/j.trgeo.2018.08.003

Connolly, D.P., Dong, K., Alves Costa, P., Soares, P., Woodward, P.K., 2020. High speed railway ground dynamics: a multi-model analysis. Int. J. Rail Transp. 8, 324–346. https://doi.org/10.1080/23248378.2020.1712267

Dassault Systems, 2018. ABAQUS. Hibbit, Karlsson Sorensen Inc., RI, USA.

Drucker, D., Prager, W., 1952. Soil mechanics and plastic analysis or limit design. Q. Appl. Math. 10, 157–165.

Esmaeili, M., Aela, P., Hosseini, A., 2017. Experimental assessment of cyclic behavior of sand-fouled ballast mixed with tire derived aggregates. Soil Dyn. Earthq. Eng.

https://doi.org/10.1016/j.soildyn.2017.03.033

Esmaeili, M., Ataei, S., Siahkouhi, M., 2020. A case study of dynamic behaviour of short span concrete slab bridge reinforced by tire-derived aggregates as sub-ballast. Int. J. Rail Transp. 8, 80–98. https://doi.org/10.1080/23248378.2019.1613938

Fathali, M., Nejad, F.M., Esmaeili, M., 2017. Influence of tire-derived aggregates on the properties of railway ballast material. J. Mater. Civ. Eng. 29, 1–9. https://doi.org/10.1061/(ASCE)MT.1943-5533.0001702

Fox, P.J., Thielmann, S.S., Sanders, M.J., Latham, C., Ghaaowd, I., McCartney, J.S., 2018. Large-scale combination direct shear/simple shear device for tire-derived aggregate. Geotech. Test. J. 41, 340–353. https://doi.org/10.1520/GTJ20160245

Ghaaowd, I., McCartney, J.S., Thielmann, S.S., Sanders, M.J., Fox, P.J., 2017. Shearing behavior of tire-derived aggregate with large particle size. I: Internal and concrete interface direct shear. J. Geotech. Geoenvironmental Eng. 143, 1–11. https://doi.org/10.1061/(ASCE)GT.1943-5606.0001775

Ghazavi, M., 2004. Shear strength characteristics of sand-mixed with granular rubber. Geotech. Geol. Eng. 22, 401–416. https://doi.org/10.1023/B:GEGE.0000025035.74092.6c

Gong, H., Song, W., Huang, B., Shu, X., Han, B., Wu, H., Zou, J., 2019. Direct shear properties of railway ballast mixed with tire derived aggregates: Experimental and numerical investigations. Constr. Build. Mater. 200, 465–473. https://doi.org/10.1016/j.conbuildmat.2018.11.284

Hall, L., 2003. Simulations and analyses of train-induced ground vibrations in finite element models. Soil Dyn. Earthq. Eng. 23, 403–413. https://doi.org/10.1016/S0267-7261(02)00209-9

Hay, W., 1982. Railroad Engineering. John Wiley & Sons Inc (US).

Ho, C., Humphrey, D., Hyslip, J., Moorhead, W., 2013. Use of recycled tire rubber to modify track-substructure interaction. Transp. Res. Rec. 119–125. https://doi.org/10.3141/2374-14

Hu, P., Zhang, C., Chen, S.J., Wang, Y., Wang, W., Duan, W.H., 2018. Dynamic responses of bridge–embankment transitions in high speed railway: Field tests and data analyses. Eng. Struct. 175, 565–576. https://doi.org/10.1016/j.engstruct.2018.08.079

Humphrey, D., Blumenthal, M., 2010. The use of tire-derived aggregate in road construction applications. Green Streets Highw. 2010 An Interact. Conf. State Art How to Achieve Sustain. Outcomes - Proc. Green Streets Highw. 2010 Conf. 389, 299–313. https://doi.org/10.1061/41148(389)25

Indraratna, B., Nimbalkar, S., 2013. Stress-strain degradation response of railway ballast stabilized with geosynthetics. J. Geotech. Geoenvironmental Eng. 139, 684–700. https://doi.org/10.1061/(ASCE)GT.1943-5606.0000758

Indraratna, B., Nimbalkar, S., Rujikiatkamjorn, C., 2014. From theory to practice in track geomechanics - Australian perspective for synthetic inclusions. Transp. Geotech. 1, 171–187. https://doi.org/10.1016/j.trgeo.2014.07.004

Indraratna, B., Sun, Q., Grant, J., 2017. Behaviour of subballast reinforced with used tyre and potential application in rail tracks. Transp. Geotech. 12, 26–36. https://doi.org/10.1016/j.trgeo.2017.08.006

Jamshidi Chenari, R., Alaie, R., Fatahi, B., 2019. Constrained compression models for tire-derived aggregate-sand mixtures using enhanced large scale oedometer testing apparatus. Geotech. Geol. Eng. 37, 2591–2610. https://doi.org/10.1007/s10706-018-00780-2

Jamshidi Chenari, R., Fatahi, B., Akhavan Maroufi, M.A., Alaie, R., 2017. An experimental and numerical investigation into the compressibility and settlement of sand mixed with TDA. Geotech. Geol. Eng. 35, 2401–2420. https://doi.org/10.1007/s10706-017-0255-3

Kaewunruen, S., Remennikov, A.M., 2008. Dynamic properties of railway track and its components: a state-of-the-art review: in book New Research on Acoustics. Res. Online Fac. Eng. Pap. Univ. Wollongong 197–220.

Kouroussis, G., Verlinden, O., Conti, C., 2011. Finite-Dynamic Model for Infinite Media: Corrected Solution of Viscous Boundary Efficiency. J. Eng. Mech. 137, 509–511. https://doi.org/10.1061/(ASCE)EM.1943-7889.0000250

Leshchinsky, B., Ling, H.I., 2013. Numerical modeling of behavior of railway ballasted structure with geocell confinement. Geotext. Geomembranes 36, 33–43. https://doi.org/10.1016/j.geotexmem.2012.10.006

Li, D., Hyslip, J., Sussmann, T., Chrismer, S., 2016. Railway geotechnics. CRC Press. https://doi.org/10.1201/b18982

Lysmer, J., Kuhlemeyer, R.L., 1969. Finite dynamic model for infinite media. J. Eng. Mech. Div. 95, 859–878.

Meena, N.K., Nimbalkar, S., Fatahi, B., Yang, G., 2020. Effects of soil arching on behavior of pile-supported railway embankment: 2D FEM approach. Comput. Geotech. 123, 103601. https://doi.org/10.1016/j.compgeo.2020.103601

Meles, D., Bayat, A., Soleymani, H., 2013. Compression behavior of large-sized tire-derived aggregate for embankment application. J. Mater. Civ. Eng. 25, 1285–1290. https://doi.org/10.1061/(ASCE)MT.1943-5533.0000675

Meles, D., Chan, D., Yi, Y., Bayat, A., 2016. Finite-element analysis of highway embankment

made from tire-derived aggregate. J. Mater. Civ. Eng. 28, 1–8. https://doi.org/10.1061/(ASCE)MT.1943-5533.0001371

Mills, B., McGinn, J., 2010. Design, construction, and performance of a highway embankment failure repaired with tire-derived aggregate. Transp. Res. Rec. J. Transp. Res. Board 2170, 90–99. https://doi.org/10.3141/2170-11

Milne, D.R.M., Le Pen, L.M., Thompson, D.J., Powrie, W., 2017. Properties of train load frequencies and their applications. J. Sound Vib. 397, 123–140. https://doi.org/10.1016/j.jsv.2017.03.006

Navaratnarajah, S.K., Indraratna, B., 2017. Use of rubber mats to improve the deformation and degradation behavior of rail ballast under cyclic loading. J. Geotech. Geoenvironmental Eng. 143, 1–47. https://doi.org/10.1061/(ASCE)GT.1943-5606.0001669

Ni, P., Qin, X., Yi, Y., 2018. Numerical study of earth pressures on rigid pipes with tire-derived aggregate inclusions. Geosynth. Int. 25, 494–506. https://doi.org/10.1680/jgein.18.00013

Nimbalkar, S., Indraratna, B., 2016. Improved performance of ballasted rail track using geosynthetics and rubber shockmat. J. Geotech. Geoenvironmental Eng. 142, 04016031. https://doi.org/10.1061/(ASCE)GT.1943-5606.0001491

Nimbalkar, S., Indraratna, B., Dash, S.K., Christie, D., 2012. Improved performance of railway ballast under impact loads using shock mats. J. Geotech. Geoenvironmental Eng. 138, 281–294. https://doi.org/10.1061/(ASCE)GT.1943-5606.0000598

Pelisser, F., Zavarise, N., Longo, T.A., Bernardin, A.M., 2011. Concrete made with recycled tire rubber: Effect of alkaline activation and silica fume addition. J. Clean. Prod. 19, 757–763. https://doi.org/10.1016/j.jclepro.2010.11.014

Ramos, A., Gomes Correia, A., Calçada, R., Alves Costa, P., Esen, A., Woodward, P.K.,

Connolly, D.P., Laghrouche, O., 2021. Influence of track foundation on the performance of ballast and concrete slab tracks under cyclic loading: Physical modelling and numerical model calibration. Constr. Build. Mater. 277, 122245. https://doi.org/10.1016/j.conbuildmat.2021.122245

Rodríguez, L.M., Arroyo, M., Cano, M.M., 2018. Use of tire-derived aggregate in tunnel cut-and-cover. Can. Geotech. J. 55, 968–978. https://doi.org/10.1139/cgj-2017-0446

Sainz-Aja, J., Pombo, J., Tholken, D., Carrascal, I., Polanco, J., Ferreño, D., Casado, J., Diego, S., Perez, A., Filho, J.E.A., Esen, A., Cebasek, T.M., Laghrouche, O., Woodward, P., 2020. Dynamic calibration of slab track models for railway applications using full-scale testing. Comput. Struct. 228, 106180. https://doi.org/10.1016/j.compstruc.2019.106180

Schilder, R., Diederich, D., 2007. Installation quality of slab track – a decisive factor for maintenance. RTR Spec. Austria 76–78.

Sheng, X.W., Zheng, W.Q., Zhu, Z.H., Luo, T.J., Zheng, Y.H., 2020. Properties of rubber under-ballast mat used as ballastless track isolation layer in high-speed railway. Constr. Build. Mater. 240. https://doi.org/10.1016/j.conbuildmat.2019.117822

Sol-Sánchez, M., Moreno-Navarro, F., Rubio-Gámez, M.C., 2015a. The use of elastic elements in railway tracks: A state of the art review. Constr. Build. Mater. 75, 293–305. https://doi.org/10.1016/j.conbuildmat.2014.11.027

Sol-Sánchez, M., Moreno-Navarro, F., Rubio-Gámez, M.C., 2014. Viability analysis of deconstructed tires as material for rail pads in high-speed railways. Mater. Des. 64, 407–414. https://doi.org/10.1016/j.matdes.2014.07.071

Sol-Sánchez, M., Thom, N.H., Moreno-Navarro, F., Rubio-Gámez, M.C., Airey, G.D., 2015b. A study into the use of crumb rubber in railway ballast. Constr. Build. Mater. 75, 19–24. https://doi.org/10.1016/j.conbuildmat.2014.10.045

Song, W., Huang, B., Shu, X., Wu, H., Gong, H., Han, B., Zou, J., 2019. Improving damping properties of railway ballast by addition of tire-derived aggregate. Transp. Res. Rec. 2673, 299–307. https://doi.org/10.1177/0361198119839345

Sun, Y., Nimbalkar, S., Chen, C., 2018. Grading and frequency dependence of the resilient modulus of ballast. Geotech. Lett. 8, 305–309. https://doi.org/10.1680/jgele.18.00084

Wolf, J.P., Song, C., 1996. Finite-element modelling of unbounded media, John Wiley and Sons. Hoboken, New Jersey.

Wolfe, S., Humphrey, D., 2000. Vibration attenuation of tire shreds. Rail Transit Conf. St Louis, MI.

Woodward, P.K., Kennedy, J., Laghrouche, O., Connolly, D.P., Medero, G., 2014. Study of railway track stiffness modification by polyurethane reinforcement of the ballast. Transp. Geotech. 1, 214–224. https://doi.org/10.1016/j.trgeo.2014.06.005

Zhou, S., 1995. Research on design parameters of bridge and tunnel in high speed railway. Beijing Minist. Railw. Acad. Sci.

Appendix

Drucker-Prager Model

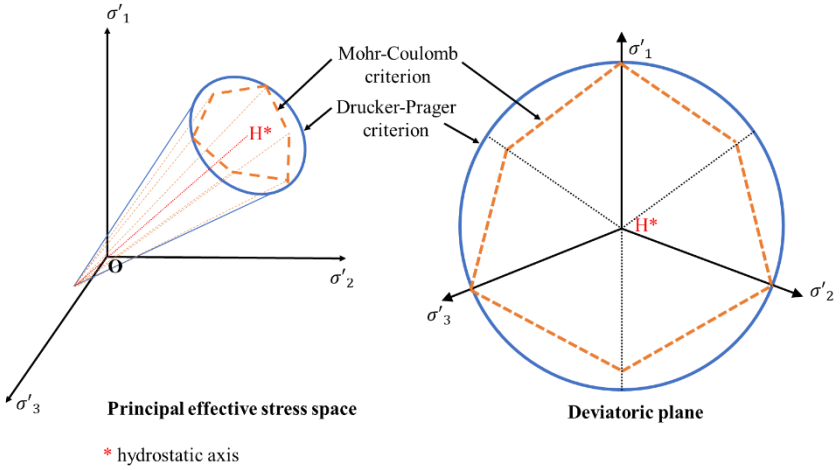

Figure A-1. Representation of yield surface for Mohr-Coulomb and Drucker-Prager model.

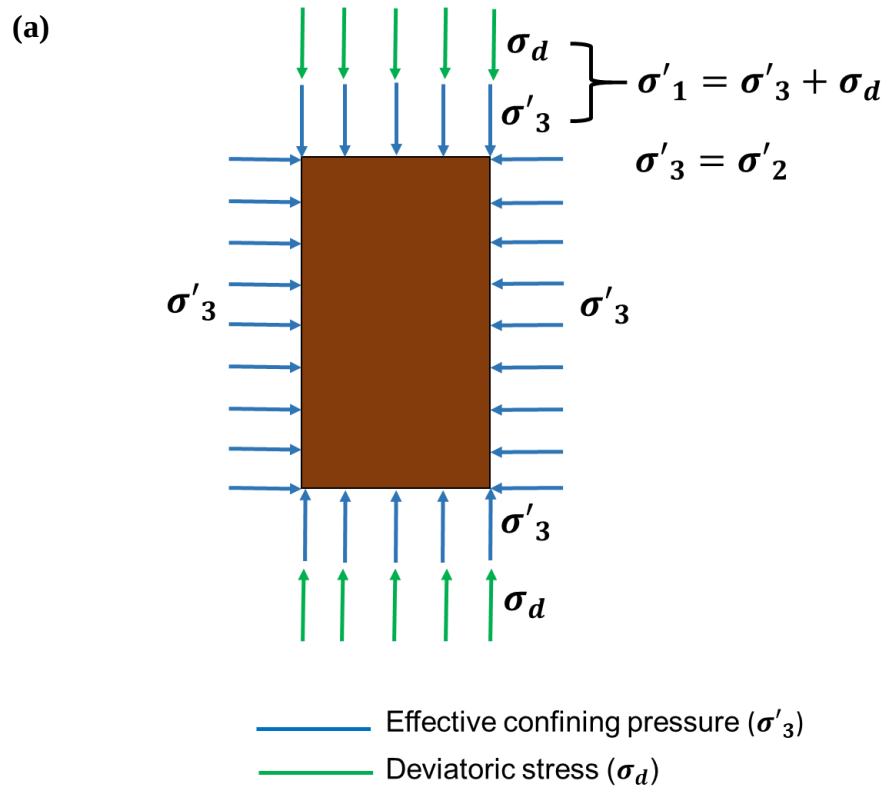

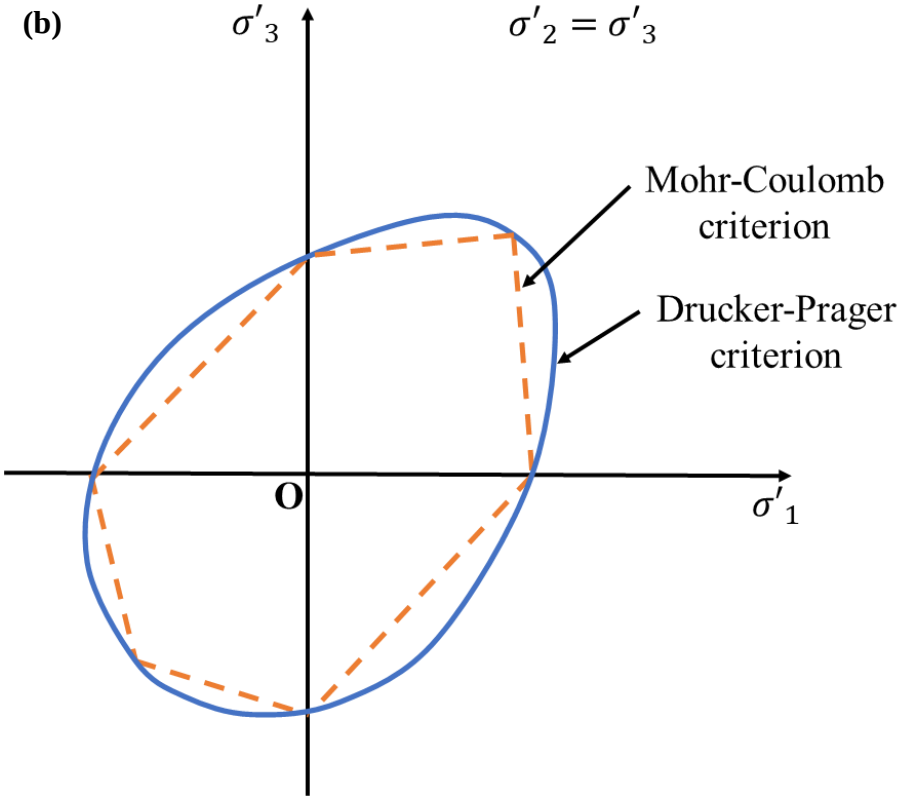

Figure A-2 (a) Axisymmetric representation of a conventional triaxial test (b) Drucker-Prager yield surface representation for axisymmetric configuration.

The Drucker-Prager (D-P) failure criterion is a generalisation of the Mohr-Coulomb (M-C) criterion for soils and is expressed in equation A-1 (Drucker and Prager, 1952). The D-P criterion has a smooth yield surface in comparison to the M-C criterion. The yield surface for M-C and D-P criterion in the principal effective stress space and the deviatoric plane is shown in Figure A-1. The sharp corners of irregular hexagon associated with a M-C criterion may cause convergence problems during numerical simulation (Alejano and Bobet, 2012).

$$\sqrt{J_2} = \alpha I'_1 + \beta \quad \text{A-1}$$

where α and β are material constants; J_2 and I'_1 are the second invariant of the deviatoric stress tensor and first invariant of the stress tensor; respectively and are represented by equations A-2 and A-3, respectively.

$$I'_1 = \sigma'_1 + \sigma'_2 + \sigma'_3 \quad \text{A-2}$$

$$J_2 = \frac{1}{6}[(\sigma'_1 - \sigma'_2)^2 + (\sigma'_1 - \sigma'_3)^2 + [(\sigma'_2 - \sigma'_3)^2] \quad \text{A-3}$$

where σ'_1, σ'_2, and σ'_3 are the principal effective stresses.

Following the D-P criterion, octahedral shear stress is expressed in terms of principal effective stress as given below.

$$\tau_{oct} = \frac{1}{3}\sqrt{[(\sigma'_1 - \sigma'_2)^2 + (\sigma'_1 - \sigma'_3)^2 + (\sigma'_2 - \sigma'_3)^2]} \quad \text{A-4}$$

For the axisymmetric stress state in a conventional triaxial test shown in Figure A-2(a), the yield surface for D-P criterion is illustrated in Figure A-2(b). Hence, for axisymmetric stress state equations A-2, A-3 and A-4 simply to equations A-5, A-6 and A-7, respectively.

$$I'_{1,axi} = \sigma'_1 + 2\sigma'_3 \quad \text{A-5}$$

$$J_{2,axi} = \frac{1}{3}(\sigma'_1 - \sigma'_3)^2 \quad \text{A-6}$$

$$\tau_{oct,axi} = \frac{\sqrt{2}}{3}(\sigma'_1 - \sigma'_3) \quad \text{A-7}$$

where, $J_{2,axi}$ and $I'_{1,axi}$ are the second invariant of the deviatoric stress tensor and first invariant of the stress tensor, respectively, for axisymmetric condition; $\tau_{oct,axi}$ is the octahedral stress for an axisymmetric condition; σ'_1 and σ'_3 are the major and minor effective principal stresses, respectively.

Hyperelastic model

A hyperelastic (HE) model is a type of constitutive model for ideally elastic materials, and the stress-strain relationship for such models is described in terms of strain energy potential (U).

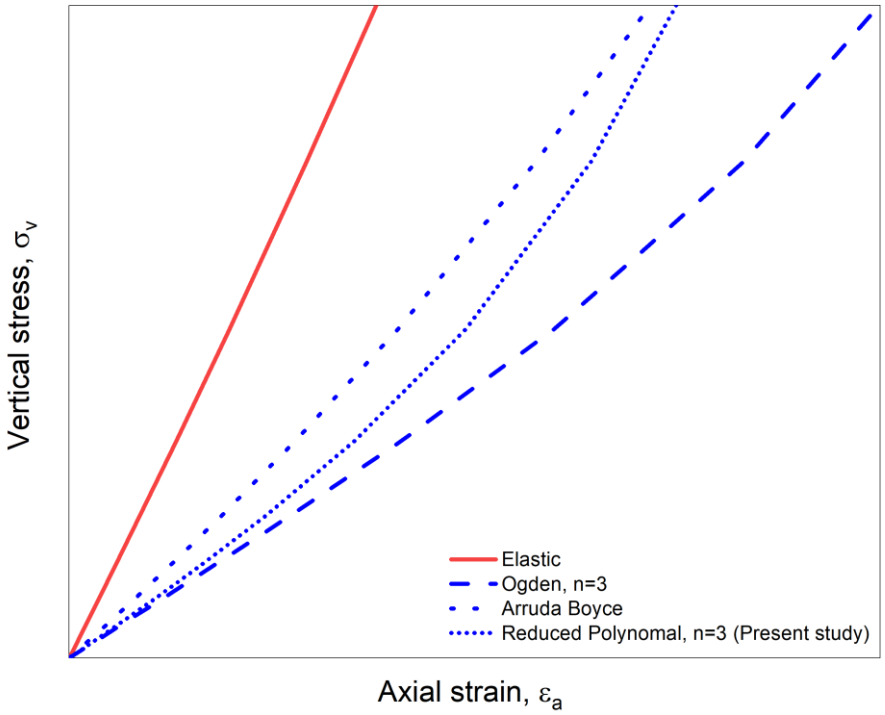

Figure A-3. Comparison of stress-strain behaviour of elastic model with hyperelastic models.

The comparison of the stress-strain behaviour of various hyperelastic models with an elastic model is shown in Figure A-3. The reduced polynomial strain energy potential is represented by equation A-8 (Abaqus Online Documentation, 2018).

$$U = \sum_{i=1}^{n} C_{i0}(\bar{I}_1 - 3)^i + \sum_{i=1}^{n} \frac{1}{D_i} (J^{el} - 1)^{2i} \quad \text{A-8}$$

where U is the strain energy per unit of reference volume; n is a material parameter; C_{i0} and D_i are temperature-dependent material parameters; $\bar{I}_1$ is the first deviatoric strain invariant which is represented by equation A-9; J^{el} is the elastic volume ratio

$$\bar{I}_1 = \bar{\lambda}_1^2 + \bar{\lambda}_2^2 + \bar{\lambda}_3^2 \quad \text{A-9}$$

The deviatoric stretches ($\bar{\lambda}_i$) is given by equation A-10

$$\bar{\lambda}_i = J^{-\frac{1}{3}} \lambda_i \quad \text{A-10}$$

where J is the total volume ratio; λ_i are the principal stretches. The initial shear modulus (constant elastic shear modulus) and effective bulk modulus are given by equations A-11 and A-12, respectively.

$$G_0 = 2C_{10} \tag{A-11}$$

$$K'_0 = \frac{2}{D_1} \tag{A-12}$$

Yeoh strain energy potential is a case of reduced polynomial strain energy potential with *n*=3. Using *n*=3 in equation A-8, the strain energy per unit of reference volume (U) is given by equation A-13.

$$U = C_{10}(\bar{I}_1 - 3) + C_{20}(\bar{I}_1 - 3)^2 + C_{30}(\bar{I}_1 - 3)^3 + \frac{1}{D_1}(J^{el} - 1)^2 + \frac{1}{D_2}(J^{el} - 1)^4 + \frac{1}{D_3}(J^{el} - 1)^6 \tag{A-13}$$

where C_{10}, C_{20}, C_{30}, D_1, D_2, and D_3 are temperature-dependent material parameters; $\bar{I}_1$ is the first deviatoric strain invariant which is represented in equation A-10; J^{el} is the elastic volume ratio.

The Ogden strain energy potential is represented in equation A-14

$$U = \sum_{i=1}^{n} \frac{2\mu_i}{\alpha_i^2}\left(\lambda_1^{-\alpha_i} + \lambda_2^{-\alpha_i} + \lambda_3^{-\alpha_i} - 3\right) + \sum_{i=1}^{n} \frac{1}{D_i}(J^{el} - 1)^{2i} \tag{A-14}$$

where μ_i, α_i, and D_i are temperature-dependent material parameters.

The Arruda-Boyce strain energy potential is represented in equation A-15

$$U = G\left\{\frac{1}{2}(\bar{I}_1 - 3) + \frac{1}{20\lambda_m^2}\left(\bar{I}_1^{\,2} - 9\right) + \frac{11}{1050\lambda_m^4}\left(\bar{I}_1^{\,3} - 27\right) + \frac{19}{7000\lambda_m^6}\left(\bar{I}_1^{\,4} - 81\right) + \frac{519}{673750\lambda_m^8}\left(\bar{I}_1^{\,5} - 243\right)\right\} + \frac{1}{D}\left(\frac{J_{el}^2 - 1}{2} - lnJ_{el}\right) \tag{A-15}$$

The relation between initial shear modulus (G_0) and shear modulus (G) is expressed in equation A-16

$$G_0 = G\left(1 + \frac{3}{5\lambda_m^2} + \frac{99}{175\lambda_m^4} + \frac{513}{875\lambda_m^6} + \frac{42039}{67375\lambda_m^8}\right) \tag{A-16}$$

where λ_m is the material constant with a typical value of 7.